International Journal of Fatigue 194 (2025) 108821

Contents lists available at ScienceDirect

International Journal of Fatigue

journal homepage: www.elsevier.com/locate/ijfatigue

A TCD-based statistical method to assess the impact of surface roughness and pores on the fatigue strength of LPBF Inconel 718 specimens

Lorenzo Romanelli [a], Ciro Santus [a,*], Giuseppe Macoretta [a], Michele Barsanti [a], Bernardo Disma Monelli [a], Ivan Senegaglia [a], Adrian Hugh Alexander Lutey [b], Hossein Rajaei [c], Cinzia Menapace [c], Matteo Benedetti [c]

[a] DICI, Department of Civil and Industrial Engineering, University of Pisa, Largo Lucio Lazzarino 1 56122, Pisa, Italy
[b] DIA, Department of Engineering and Architecture, University of Parma, Parco Area delle Scienze 181/A 43124, Parma, Italy
[c] DII, Department of Industrial Engineering, University of Trento, Via Sommarive 9 38123, Trento, Italy

ARTICLE INFO

Keywords:
Laser powder bed fusion
Surface roughness
Internal pores
Extreme value statistics
Theory of critical distances

ABSTRACT

The aim of this study is to model the impact of surface roughness and pores on the fatigue strength of plain and V-notched specimens made of Inconel 718 under as-built and machined conditions and produced by laser powder bed fusion (LPBF). Combining fractographic analyses with the Gumbel and the exponential distribution functions, the statistical analyses of the diameters of the pores and of their distances from the external surfaces were implemented. Surface roughness scans were performed with the optical profilometer. The finite element (FE) method was used to simulate a sample of pores generated by the identified probability distributions and the surface profiles obtained with the scans. The theory of critical distances (TCD) was implemented combining the blunt and sharp V-notched specimens in the machined condition, and it was combined with the Gumbel or the generalized extreme values distributions to calculate the fatigue strength concentration factors provided by the pores and the surface roughness at 99% of probability. Finally, the proposed model was used to predict the fatigue strength of the blunt V-notched specimens in the as-built conditions and of the plain specimens in the as-built and machined conditions resulting appreciably similar to the experimental data.

1. Introduction

Additive manufacturing (AM) has seen tremendous growth in recent years, revolutionizing the production of complex geometries and high-performance materials. One of the most widely used materials in AM is Inconel 718, a nickel-based superalloy known for its excellent mechanical properties [1]. These properties include high tensile strength, superior corrosion resistance, and the ability to retain mechanical integrity at elevated temperatures, making it ideal for applications that demand extreme material performance. Inconel 718's exceptional strength-to-weight ratio and its ability to withstand temperatures as high as 700 °C make it an indispensable material for industries such as aerospace, automotive, energy, and defense [2–5]. The aerospace sector, in particular, has benefited from AM technology, which allows for the production of lightweight, complex, and highly integrated components [6,7]. Inconel 718 is often used in the production of turbine blades, heat shields, and other high-stress components in jet engines due to its ability to endure high thermal and mechanical stresses over extended periods of time. The flexibility of AM processes, particularly LPBF and electron beam powder bed fusion (EB-PBF), has opened new opportunities to produce intricate geometries that were previously unachievable through conventional subtractive manufacturing methods [8,9]. The potential to reduce material wastage, minimize lead times, and improve design flexibility has led to the widespread adoption of AM in the production of Inconel 718 components for high-performance applications [10]. However, while the promise of AM to create geometrically complex, high-performance components is undeniable, challenges persist, particularly with regard to the introduction of defects during the manufacturing process. These defects can have significant consequences for the mechanical performance of components, especially in critical applications where reliability is paramount [11–13]. One of the most significant challenges in AM processes, particularly with materials like Inconel 718, is the formation of defects such as surface roughness and internal porosity [14,15]. These defects arise as a result of the layer-by-layer nature of AM, where each layer is built by melting and solidifying powder particles using a high-energy source such as a laser or electron beam. Variations in the energy

* Corresponding author.
E-mail address: ciro.santus@unipi.it (C. Santus).

https://doi.org/10.1016/j.ijfatigue.2025.108821
Received 28 October 2024; Received in revised form 20 December 2024; Accepted 13 January 2025
Available online 18 January 2025

Nomenclature

LPBF	Laser powder bed fusion
FE	Finite element
TCD	Theory of critical distances
AM	Additive Manufacturing
EB-PBF	Electron beam powder bed fusion
E_{d}	Energy density
S_{sk}	Areal Skewness parameter to describe the symmetry of the scanned portion with respect to the mean surface
S_{ku}	Areal Kurtosis parameter to describe the sharpness of the roughness profile
FL	Fatigue limit
LM	Line method
FSCF	Fatigue stress concentration factor
PM	Point method
L	Critical distance calculated with line method
L'	Critical distance calculated with point method
EVS	Extreme value statistics
a_{eff}	Effective defect/crack size
$area$	Area of internal defects according to the Murakami model
p	Pitch distance between two consecutive roughness valleys
a	Crack depth of fracture mechanics readapted to valley depth in the Murakami model
S_{v}	Areal roughness parameter indicating the maximum valley depth
R_{sm}	Mean spacing of a profile element widths
CT	Computed tomography
SEM	Scanning electron microscope
ICP-OES	Inductively coupled plasma optical emission spectrometry
PSD	Particle size distribution
VR02	Sharp V-notched specimen with a nominal notch radius equal to 0.2 mm
VR1	Blunt V-notched specimen with a nominal notch radius equal to 1 mm
R_{N}	Notch radius
BD	Build direction
P	Laser power
v	Scan velocity
h	Hatch distance
t	Layer thickness
A_{r}	Meltpool aspect ratio
B_{r}	LPBF build rate
a_{t}	Cutting depth
f_{t}	Feed rate
v_{t}	Cutting speed
R_{a}	Monodimensional roughness parameter indicating the arithmetical mean height
E	Young modulus
S_{Y}	Yield strength
S_{U}	Ultimate strength
ε_{f}	Percent elongation at fracture
μ_{t}	Mean value of the quantities obtained from monotonic tensile test
σ_{t}	Standard deviation of the quantities obtained from monotonic tensile test
R	Stress ratio of the fatigue tests
σ_{a}	Stress amplitude
k and b	Basquin parameters
N_{f}	Number of cycles to failure
N	Number of experimental data
$\sigma_{\mathrm{a},i}$	$I-$th value of the experimental stress amplitude data
$\hat{\sigma}_{\mathrm{a,i}}$	Estimated value of the $i-$th experimental stress amplitude according to the fitted curve
q	Number of parameters of the fitted curve
OM	Optical microscope
G	Grain size number according to ASTM E112
$A_{\mathrm{r,g}}$	Grain aspect ratio
MC	Metal carbides
$D_{\mathrm{pl,max}}$	Maximum diameter in each fractographic scan for the plain specimen
$D_{\mathrm{N,max}}$	Maximum diameter in each fractographic scan for the V-notched specimen
d_{pl}	Distance of the maximum pore of a cross-section of the plain specimen from the external surface
d_{N}	Distance of the maximum pore of a cross-section of the VR1 specimen from the external surface
x, y	Random variables
μ_x, μ_y	Average of the random variables x and y
r	Pearson correlation factor
$\mathrm{R}[x]$, $\mathrm{R}[y]$	Rank variables of the random variables x and y
r_{s}	Spearman correlation factor
r_{k}	Kendall correlation factor
F_{G}	Distribution function of Gumbel
F_{E}	Exponential distribution function
F_{V}	Generalized extreme value distribution function
i	Position of the $i-$th experimental data sorted in ascending order
a, b	Parameters of the distribution function of Gumbel
μ	Parameter of the exponential distribution function
ζ, μ_{gev}, σ_{gev}	Parameters of the generalized extreme value distribution function
ΔK_{th}	Threshold stress intensity factor range
D	Bar diameter i.e. the gros diameter of the V-notched specimens
$\sigma_{\mathrm{VR02,m,a}}$	Fatigue strength of the machined VR02 specimen
σ_{a}^{*}	Fatigue strength of the intrinsic plain specimen according to line method

$\sigma_{a}^{*\prime}$	Fatigue strength of the intrinsic plain specimen according to point method
$\sigma_{a,VR1}^{*}$	Fatigue strength of the intrinsic VR1 specimen
$\sigma_{pl,a}$	Fatigue strength of the plain as-built specimen
$\sigma_{pl,m,a}$	Fatigue strength of the plain machined specimen
R_{02}	Measured notch radius of the sharp V-notched specimen
$\sigma_{VR1,m,a}$	Fatigue strength of the machined VR1 specimen
$\sigma_{VR1,a}$	Fatigue strength of the as-built VR1 specimen
R_{1}	Measured notch radius of the blunt V-notched specimen
D_{02}	Measured bar diameter of the sharp V-notched specimen
D_{1}	Measured bar diameter of the blunt V-notched specimen
σ_{x}	Axial stress
A, B	Parameters of the curve describing the dependence of the critical distance obtained with line method on the number of cycles
A_{1}, B_{1}	Parameters of the curve describing the dependence of the critical distance obtained with point method on the number of cycles
$K_{f,rough}$	FSCF provided by the surface roughness according to line method
$K'_{f,rough}$	FSCF provided by the surface roughness according to point method
$K_{f,pl,pore}$	FSCF provided by the pore in the as-built and machined plain specimens according to line method
$K'_{f,pl,pore}$	FSCF provided by the pore in the as-built and machined plain specimens according to point method
$K_{f,N}$	FSCF provided by the notch in the blunt V-notched specimen according to line method
$K'_{f,N}$	FSCF provided by the notch in the blunt V-notched specimen according to point method
$K_{f,VR1,pore}$	FSCF provided by the pore in the machined V-notched specimen according to line method
$K'_{f,VR1,pore}$	FSCF provided by the pore in the machined V-notched specimen according to point method
$K_{f,pl,rough}$	FSCF provided by the surface roughness according to line method in the as-built plain specimen
$K'_{f,pl,rough}$	FSCF provided by the surface roughness according to point method in the as-built plain specimen
$K_{f,plm,rough}$	FSCF provided by the surface roughness according to line method in the machined plain specimen
$K_{f,VR1,rough}$	FSCF provided by the surface roughness according to line method in the as-built V-notched specimen
$K_{f,pl,tot}$	Total FSCF according to line method for the as-built plain specimen
$K'_{f,pl,tot}$	Total FSCF according to point method for the as-built plain specimen
$K_{f,VR1,tot}$	Total FSCF according to line method for the as-built V-notched specimen
$K_{f,plm,tot}$	Total FSCF according to line method for the machined plain specimen
$K_{f,VR1\ m,tot}$	Total FSCF according to line method for the machined V-notched specimen
$N_{f,pred}$	Predicted number of cycles to failure
$\sigma_{a,pred}$	Predicted fatigue strength
$\sigma_{a,pred,pl}$	Predicted fatigue strength of the plain as-built specimen with line method
$\sigma'_{a,pred,pl}$	Predicted fatigue strength of the plain as-built specimen with point method
$\sigma_{a,pred,plm}$	Predicted fatigue strength of the plain machined specimen with line method
$\sigma_{a,pred,VR1}$	Predicted fatigue strength of the as-built VR1 specimen with line method
$\sigma_{a,pred,VR1m}$	Predicted fatigue strength of the machined VR1 specimen with line method

input, powder bed quality, and cooling rates can lead to incomplete fusion of particles, resulting in voids (porosity) within the material and irregular surface textures. Surface roughness in additively manufactured parts can significantly affect their mechanical performance, particularly their fatigue behaviour. Rough surfaces act as stress concentrators, making it easier for cracks to initiate under cyclic loading conditions. These cracks then propagate through the material, leading to premature failure. For example, in Inconel 718 parts produced via LPBF, as-built surfaces are typically rough due to the unmelted powder particles and irregular melting patterns. Witkin et al. found that surface features as small as 50 μm can act as crack initiation sites, significantly reducing the fatigue limit (FL) of the material [16]. Post-processing techniques like surface polishing or machining are often employed to smooth these surfaces, but these additional steps increase costs and processing times. Internal porosity is another critical defect that affects the structural integrity of additively manufactured components. These voids form due to inadequate energy input during the melting process or the formation of keyhole defects, where excessive energy causes vaporization of the material creating pores. Internal pores can serve as crack initiation points under cyclic loading, compromising the component's fatigue life. Guo et al. demonstrated in Ref. [17] that adjusting key process parameters such as laser power, scan speed, and hatch spacing can reduce the formation of pores and cracks in LPBF fabricated Inconel 738LC parts. Their study identified an optimal energy density E_d of 48 J/mm^3, which minimized defects and improved the mechanical performance of the parts. Additionally, Stopka et al. in Ref. [18] investigated the porosity of LPBF Inconel 718 specimens, and they obtained that a value of E_d between 62 and 79 J/mm^3 can minimize the internal porosity. As concerns the surface morphology, Uriati et al. highlighted in Ref. [19] that surface roughness parameters, such as skewness (S_{sk}) and kurtosis (S_{ku}), play a crucial role in determining fatigue resistance in as-built Inconel 718 parts. They found that parts with higher skewness and kurtosis values exhibited lower fatigue strength, underscoring the need for optimized surface quality in AM-produced components. In recent years, researchers have shifted their approach to understanding the impact of AM-induced defects on fatigue performance. Instead of treating surface roughness and internal porosity as separate entities, these defects are increasingly being reinterpreted as micro-notches that act as stress concentrators. This approach recognizes that both surface irregularities and internal voids can raise local stress levels in the material, which in turn facilitates crack initiation under cyclic loading [20–23].

TCD has emerged as a valuable tool in quantifying the effect of micro-notches on fatigue strength. TCD introduces a material characteristic length scale that determines the material's tolerance to stress concentrations caused by defects. When the characteristic length of a material is known, it becomes possible to predict whether a stress concentration from a defect, such as a micro-notch, will lead to crack initiation [24]. TCD has two principal formulations i.e. the line method (LM) and the point method (PM) [25]; the LM identifies the fatigue stress concentration factor (FSCF) of a notch by averaging the stress distribution along the notch bisector over the distance $2L$ where L is the critical distance, while the PM identifies the FSCF by evaluating the stress at a certain distance ($L'/2$) from the notch apex. The TCD was also formulated as the area method and the volume method, where the stress is averaged over an area and a volume, respectively. The LM and the PM have been widely employed over the years to assess the fatigue strength of notched components produced with traditional technologies as in Refs. [26–29], and it has also been employed with critical plane criteria as the Smith-Watson-Topper criterion [30] in Refs. [31,32] or the Fatemi–Socie criterion [33,34] in Refs. [32,35]. In addition, crystal plasticity theory was recognized by He et al. in Ref. [36] as a valid tool to be used in fatigue strength investigations, and in the same research it was combined with Tanaka-Mura-Wu fatigue model [37]. Given the key role of crystal plasticity theory in describing the constitutive behaviour of the material at grain size, it was also coupled with TCD by He et al. in Ref. [38] to study the microstructural and size effects on fatigue strength of notched components made of GH4169 alloy. Recently, the application of TCD has been also extended to AM materials as Ti-6Al-4V in Ref. [10] by Benedetti et al. In this study it has been demonstrated that defects located near notch tips can significantly influence fatigue crack initiation and propagation. Their research used the inverse critical distance search method, proposed in Ref. [39] by Santus et al. which enabled them to predict notch fatigue strength, even in scenarios where the material exhibited high defect sensitivity. One of the most important aspects of predicting the fatigue strength of AM components is understanding the mutual interaction between surface roughness and internal porosity, especially when internal defects are located close to the surface. In such cases, the interaction between these defects can significantly amplify local stress concentrations, further reducing the fatigue strength of the component. In the literature there are some examples about the use of TCD to predict fatigue strength of specimens, made for example of Ti-6Al-4V and obtained by LPBF, by accounting for the interacting effects of surface roughness and porosity as presented in Gillham et al. [40] and Dinh et al. [41], where accurate fatigue strength predictions were obtained.

Alternatively, the Murakami model [42] is a strong and efficient method to investigate the fatigue strength of mechanical components as described by Santus et al. in Ref. [43] and by Chapetti in Ref. [44]. This model is based on the $\sqrt{area}$ parameter, and it can be used to assess fatigue strength of additive manufacturing components. For example, in Zhang and Fatemi [45], Macoretta et al. [46] and Rigon et al. [47] the $\sqrt{area}$ was calculated according to the expression proposed by Murakami in Ref. [42] and described in Eq. (1), which aims to make an equivalence between the defects and the surface roughness. In Eq. (1) a and p represent the valley depth of the rough profile and the pitch between roughness valleys, respectively. In particular in Ref. [47] the dimension of a_{eff}, which represents the effective crack length, was obtained with three different methods. In the first proposal the authors considered that $a_{\text{eff}} = 0.65^2\sqrt{area}$, where $\sqrt{area}$ was calculated according to Eq. (1), the parameter a was calculated as S_v, thus the areal roughness parameter indicating the maximum valley depth according to ISO 25178–2, p was identified as R_{sm}, thus the mean spacing of a profile element widths according to ISO 4287:1997 and 0.65^2 is for surface defects. In the second approach, a_{eff} was computed with the expression proposed by Murakami in Ref. [42] for very shallow crack, i.e. $a_{\text{eff}} = \sqrt{10}S_v$. Finally, in the third approach the authors used the maximum obtained value of S_v, and the value of the effective crack length was calculated as $a_{\text{eff}} = 0.728^2 S_v$, where 0.728 is a multiplicative coefficient proposed by Newman and Raju in Ref. [48]. The parameter S_v was obtained by means of an optical profilometer, and the extreme value statistics (EVS) was employed to obtained the largest value of S_v. After the determination of the quantity a_{eff}, fatigue strength predictions were performed on a plain specimen, and it was obtained that the third method provided better level of accuracy.

$$\sqrt{area} = \begin{cases} p\left(2.97\left(\frac{a}{p}\right) - 3.51\left(\frac{a}{p}\right)^2 - 9.74\left(\frac{a}{p}\right)^3\right) & \text{if } \frac{a}{p} < 0.195 \\ 0.38p \quad \text{if } 0.195 < \frac{a}{p} < 3 & \end{cases} \tag{1}$$

In addition, in Yamashita et al. [49] the Murakami model based on the determination of the $\sqrt{area}$ parameter was employed to account for the effects of internal defects on the fatigue strength of Inconel 718 specimens produced with AM. Yamashita et al. in Ref. [50] also modelled the interaction between the internal pores and the surface roughness with the $\sqrt{area}$ parameter. In this latter study, they applied the $area$ parameter model and extreme value statistics to predict the fatigue behaviour of Inconel 718 produced via LPBF. They found that surface defects in contact with the material's surface had an enlarged effective size due to stress concentration, underscoring the critical importance of controlling surface quality during the AM process.

In industrial settings, accurately predicting the fatigue behaviour of additively manufactured components is essential to ensure their reliability in critical applications. To achieve this, a combination of non-destructive evaluation techniques and statistical models is employed. One of the most widely used techniques is computed tomography (CT) scanning, which provides detailed insights into the internal structure of AM components. CT scans enable the detection of internal defects such as pores and cracks, which are otherwise invisible through conventional surface inspections. This approach allows engineers to assess the size, shape, and distribution of internal defects through the component as highlighted by Zanini et al. in Ref. [51], by Witkin et al. in Ref. [16] and by Wang et al. in Ref. [52]. In addition to this, as demonstrated by Shahabi et al. in Ref. [53], 2D cross-sectional porosity data obtained with the optical microscope can be used to infer the defects size, shape and location in AM components. By examining metallographic sections and acquiring data with surface profilometers, engineers can gain a deeper understanding of the surface quality and internal structure of AM parts. Once the distribution of defects is known, extreme value statistics can be applied to assess the likely impact of the most critical defects on fatigue performance. Extreme value statistics focus on the behaviour of the largest or most severe defects within the material, as these are typically responsible for initiating fatigue cracks under cyclic loading. Extreme value statistics has been employed by researchers in fatigue strength prediction of materials obtained with traditional technologies as by Pedranz et al. in Ref. [54] or by Benedetti et al. in Ref. [55] and, recently, it has also been used for the fatigue strength assessment of AM specimens as by Ai et al. in Ref. [56] and by Niu et al. in Refs. [57,58]. Hosseini and Popovich's review [5] highlighted the importance of integrating non-destructive evaluation techniques with robust statistical models to predict the fatigue life of additively manufactured Inconel 718 components. Their research reinforced the need for a systematic approach to defect management, particularly in high-stress applications like aerospace, where even small defects can have catastrophic consequences.

The main point of this research concerns the proposal of a simplified, statistical and TCD-based approach to calculate the FSCFs provided by the surface roughness and the internal pores in LPBF specimens. The implemented FE simulations to study the effects of surface roughness and pores were 2D and 3D, respectively, and they were performed separately, thus reducing the complexity of a hypothetical 3D complete FE model with both pores and surface roughness. After the statistical investigation of the results of FE simulations, the obtained fatigue stress concentration factors were combined in a simple and conservative way and they were employed for fatigue strength predictions resulting in a good level of accuracy. The research was structured as follow. Firstly, fatigue tests were performed on plain and V-notched (sharp and blunt) specimens, in the as-built and machined conditions, made of Inconel 718 and produced with LPBF. Fractographic analyses were employed to inspect the internal pores of the specimens, and a statistical analysis was implemented to investigate the defect sizes and their distances from the external surface. The 3D optical profilometer, which is a powerful and recognized tool to examine the surface morphology as demonstrated by Macek et al. in Refs. [59–62], by Nicoletto et al. in Ref. [63] and by Santus et al. in Ref. [31], was then employed for surface investigations. 3D FE simulations of pores generated according to the identified probability distributions of the diameter and the distance from the external surface were implemented, and 2D FE simulations of the surface profiles obtained with the optical profilometer were performed. The critical distances, calculated with the double notch inversion, were then employed to calculate the FSCFs provided by the pores and the surface roughness. Finally, the as-built blunt V-notched specimens and the machined and as-built plain specimens were involved for fatigue strength predictions.

2. Materials

2.1. Specimen manufacturing and geometries

The Inconel 718 powder analyses were performed in terms of chemical composition and sizes. Powder chemical analysis was determined by inductively coupled plasma optical emission spectrometry (ICP-OES) according to ASTM E2594-20 standard. Carbon C and oxygen O were measured through combustion techniques in oxygen (for C) and inert gas (for O), according to the ASTM E1019-18 standard. Percentages of the chemical elements in the Inconel 718 powder are reported in Table 1. Powder analyses were also performed with the scanning electron microscope (SEM): Fig. 1 shows the virgin powder particles, which have a spherical morphology with some satellites on the surface. A cross-sectional metallographic analysis (Fig. 1(d)) reveals a typical dendritic as-cast microstructure. The powder particle size distribution (PSD) was evaluated using sieve analysis on a 100 g batch, as shown in Fig. 2. Two sieves (25 μm and 45 μm) were used, considering that most of the particles are finer than 45 μm. The results of the particle size distribution are shown in Fig. 2.

The mechanical drawings of the manufactured specimens are reported in Fig. 3. Three different types of geometries were involved in the current research:

- a sharp V-notched specimen with a nominal notch radius equal to $R_N = 0.2$ mm (VR02) shown in Fig. 3(a)
- a blunt V-notched specimen with a nominal notch radius equal to $R_N = 1$ mm (VR1) shown in Fig. 3(b)
- a plain specimen according to ASTM E466 standard shown in Fig. 3(c)

The design of the sharp and the V-notched specimens was inspired by the research of Santus et al. [39] to calculate the values of the critical distances as explained below. The specimens were manufactured with their axis aligned along the build direction (BD) as indicated in Fig. 3. The parameters of the 3D printing process were: the laser power P, the scan velocity v, the hatch distance h, the layer thickness t, the meltpool aspect ratio A_r, defined as the ratio between the length l and the diameter of the pool $2r$ ($A_r = l/2r$) where the values of l and $2r$ were defined according to Refs. [46,64], the energy density E_d defined as $E_d = P/thv$ and the LPBF build rate defined as $B_r = thv$. The values of the 3D printing parameters are reported in Table 2, and they are the same as those of our previous research: Ref. [65] and Ref. [46] for the baseline case. It was obtained by Moda et al. in Ref. [64] that the parameters reported in Table 2 can mostly prevent the presence of keyhole defects, lack of fusion and internal pores. During the printing process, the hatching area underwent a stripe scanning consisting on a rotation of 67° for each layer to minimize the possible anisotropy of the specimens. As concerns the outer regions, they were printed with 3 contouring paths parallel to the border and performed in the same direction. To prevent possible distortions of the specimens once removed from the building platform, to reduce residual stresses, to prevent oxidation and to avoid differences between the specimens, these latter were printed in a single batch with the build platform heated at 170 Celsius degrees and the process chamber was filled of Argon gas to obtain an Oxygen concentration less than 7 parts per million by weight. After the printing process, the specimens underwent an aging treatment, consistent with AMS 563 and that performed by Zhang et al. in Ref. [66], which can provide a significant increase of the hardness as demonstrated in Ref. [46]. The employed furnace chamber was filled with Argon gas to prevent oxidation. The performed aging treatment consisted of two different phases, in the first phase the specimens reached a temperature of 980 °C, which was maintained for 1 h, then they were subjected to a forced furnace cooling until 50 °C were reached. In the second phase, the specimens underwent a heating up to 720 °C, and this level of temperature was kept for 8 h, then a forced furnace cooling was applied with a decreasing temperature rate of 55 °C/h until 620 °C were reached. This latter level of temperature was maintained for 8 h, and a final air cooling was performed. The heat treatment process of the current research was also coherent with that implemented, after a 3D printing process with similar 3D printing parameters of those of this research, in Refs. [67,68]. In this latter research the residual stresses at the end of the whole process were measured obtaining almost null values. For this latter reason, the impact of the residual stresses on the fatigue strength of the specimens involved in this study was neglected.

In this research, two kinds of surface conditions were involved: the as-built and the machined. The specimens in the as-built condition did not undergo any surface treatment after the 3D printing process, while the specimens in the machined condition underwent a turning machining operation, which was performed with a CoroTurn TR insert with an ISO nomenclature TR-VB1304-F H13 A. The fatigue behaviour of the sharp V-notched specimen was investigated only in the machined surface condition, while the fatigue behaviour of the blunt V-notched and of the plain specimens was investigated under both machined and as-built surface conditions. The turning machining operation was performed after the heat treatment and the turning parameters, i.e. the cutting depth a_t, the feed rate f_t and the cutting speed v_t were the same of our previous study [65]. The zones where this machining operation was implemented are indicated in Fig. 3 where two roughness symbols are reported, one to indicate that the surface did not undergo any surface treatment while the other, reported in brackets in Figs. 3(b) and (c), indicates that the specimen underwent a machining turning operation. The reported symbols indicate the value of R_a, i.e. the monodimensional roughness parameter indicating the arithmetical mean height, which was expected to be obtained after the machining operation. In the sharp and blunt V-notched specimens the turning operation was focused on the notch zone (Figs. 3(a) and (b)), while in the plain specimens it was focused on the gauge length zone (Fig. 3(c)).

2.2. Mechanical tests

The static mechanical properties were considered isotropic, and the Young modulus E, the yield strength S_Y, the ultimate strength S_U and the percent elongation at fracture ε_f were the same as those of our previous research [46,65]. They are reported in Table 3 with the corresponding ratio between the mean value and the standard deviation obtained from tensile tests performed by Macoretta et al. in Ref. [46] on specimens manufactured with the same 3D printing parameters, and

Table 1
Percentages of the chemical elements in the Inconel 718 powder.

Cr	Ni	Fe	Mo	Nb	Ti	Al	C	Mn	Si	P	S	W	Co	Cu	O
18.7	52.7	18.6	3.1	4.99	0.98	0.44	0.059	0.06	0.14	<0.005	<0.002	<0.01	0.03	0.02	0.009

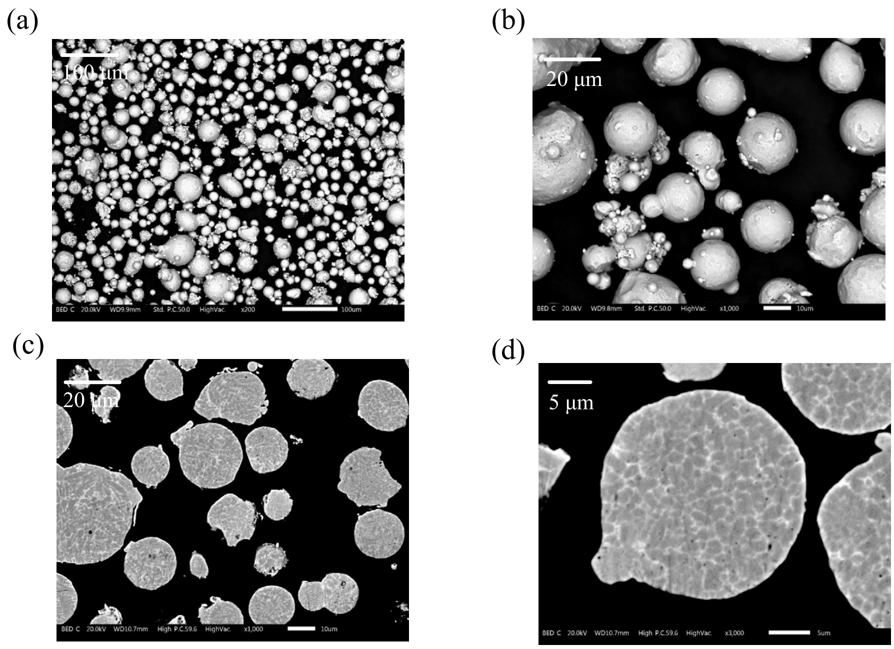

Fig. 1. SEM of Inconel 718 virgin powder.

Table 2
3D printing parameters employed in the LPBF process.

P (W)	v (m/s)	h μm	t μm	A_r –	E_d (J/mm^3)	B_r (mm^3/s)
280	0.9	90	60	5	57.6	4.9

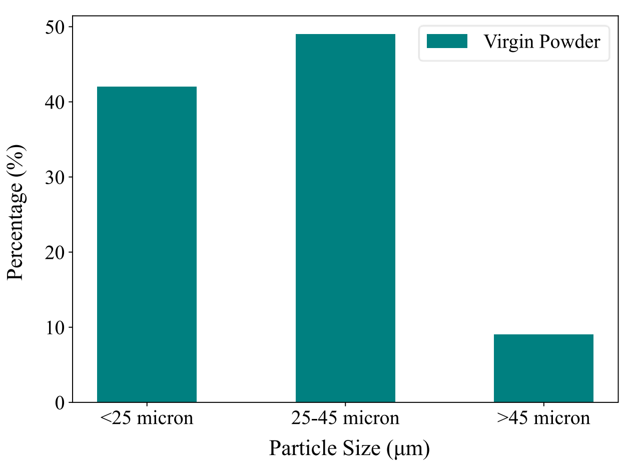

Fig. 2. Particle size distribution of Inconel 718 powder.

that underwent the same heat treatment of this research. In addition to this, a Poisson ratio equal to $\nu = 0.29$ was considered according to what obtained by Barros et al. in Ref. [67] for similar 3D printing and heat treatment processes.

In this research fatigue tests were performed at room temperature with a RUMUL Mikrotron resonant testing machine, with a testing

Table 3
Static mechanical properties of LPBF Inconel 718.

Mechanical property	μ_t	σ_t/μ_t
S_Y (MPa)	1085	1%
S_U (MPa)	1340	1%
ε_f (%)	16	10%
E (GPa)	155	3%

frequency of the order of 100 Hz, and the imposed stress ratio, defined as the ratio between the minimum and the maximum imposed nominal stress, was equal to $R = 0$. The Basquin law, described in Eq. (2), was used to fit the experimental data, and in Eq. (2), σ_a is the stress amplitude, k and b are the Basquin parameters and N_f represents the number of cycles to failure. The experimental data are presented, together with the fitted curve at 50% of probability, in Figs. 4 and 5 for the machined sharp V-notched, the machined blunt V-notched, the plain both machined and as-built and the as-built blunt V-notched specimens. The standard deviation was calculated for the fatigue curves according to Eq. (3) where N represents the number of data, $\sigma_{a,i}$ represents the i−th experimental data of the stress amplitude, $\hat{\sigma}_{a,i}$ is the estimated value of the i−th experimental data of the stress amplitude according to the fitted curve and q indicates the number of parameters of the fitted curve, which are 2 in the case of the Basquin law. The values of the standard deviation were employed to calculate the curves at 10% or 90% of probability, which are represented with dashed lines in Figs. 4 and 5. The FL was fixed at 2×10^6 number of cycles consistently with our previous research [65]. The obtained values of the Basquin parameters, the standard deviation and FL for the five types of specimens are reported in Table 4.

$$\sigma_a = k N_f^b \tag{2}$$

$$\sigma_f = \sqrt{\frac{\sum_{i=1}^{N} \left(\sigma_{a,i} - \hat{\sigma}_{a,i}\right)^2}{N - q}} \tag{3}$$

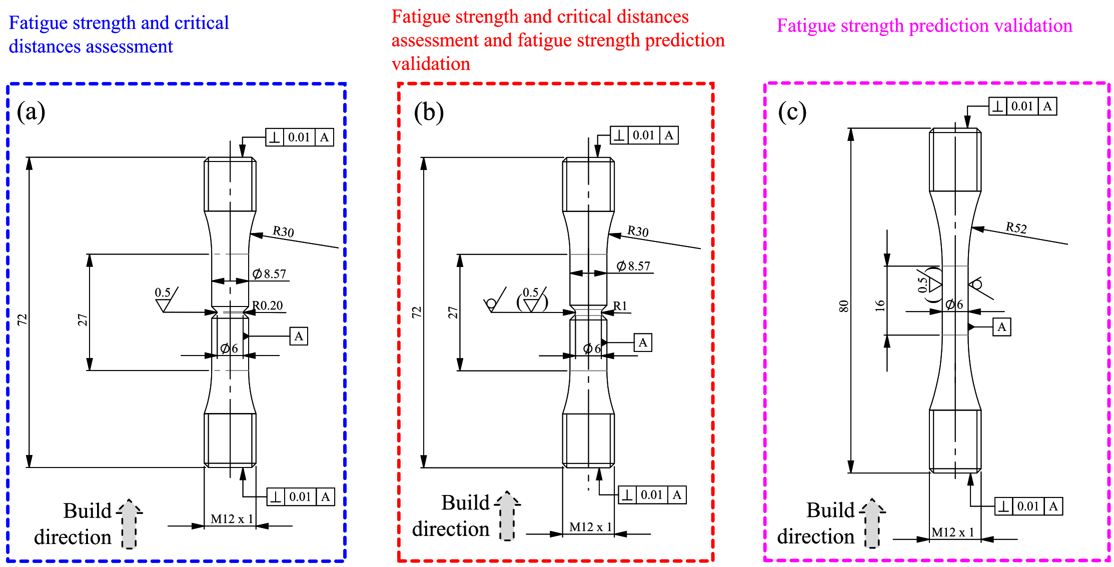

Fig. 3. Geometries and dimensions (in mm) of the 3D printed specimens involved in the research: (a) machined sharp V-notched specimen, (b) machined and as-built blunt V-notched specimen and (c) machined and as-built plain specimen.

Table 4
Numerical values obtained from the fitting operation on the experimental fatigue data.

Specimen type	Fitted Basquin law	Exp. FL (2×10^6 cycles) MPa	σ_f MPa
Sharp V-notched machined	$k = 3050$ MPa, $b = -0.230$	109	10.3
Blunt V-notched machined	$k = 6400$ MPa, $b = -0.261$	146	14.7
Cylindrical as-built	$k = 5200$ MPa, $b = -0.253$	132	10.3
Cylindrical machined	$k = 1540$ MPa, $b = -0.139$	205	19.6
Blunt V-notched as-built	$k = 2590$ MPa, $b = -0.224$	100	6.18

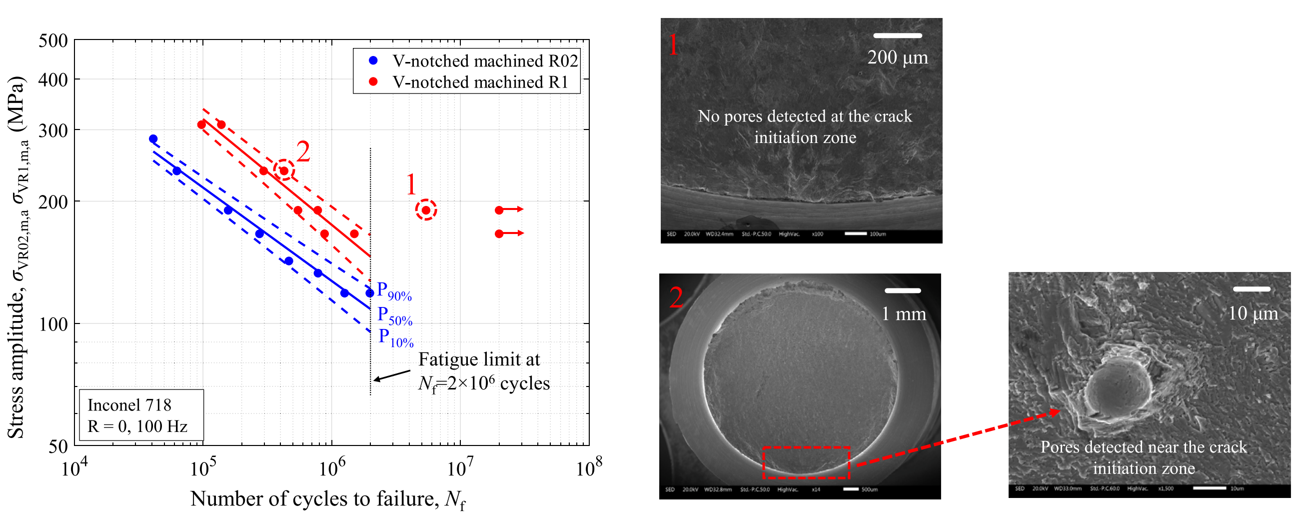

Fig. 4. SN curves of the machined VR02 ad VR1 specimens.

The Vickers hardness profile measurements were performed on a machined VR1 specimen using a Vickers microhardness tester (FM-310, FUTURE-TECH CORP). Measurements were taken with a 50 g load, with a step of 100 μm between the first two indentation points from the external surface, and then a distance of 250 μm between subsequent points. Hardness was measured in the plane where the fatigue crack occurred, which was close to the notch bisector plane, up to a distance of 3 mm from the surface along a radial path. For each point, 10 measurements were taken, and the mean value and standard deviation were calculated and reported in the graph in Fig. 6. As observed, the hardness is constant along the profile, confirming that no hardening phenomena occurred on the sample surface. Even though the results were obtained for a machined VR1 specimen, they can be generalized for all the other specimens given that the hardness depends on the material and on the performed heat treatment, which were the same for all the specimens. The obtained values of hardness are coherent with those obtained in our previous research [65].

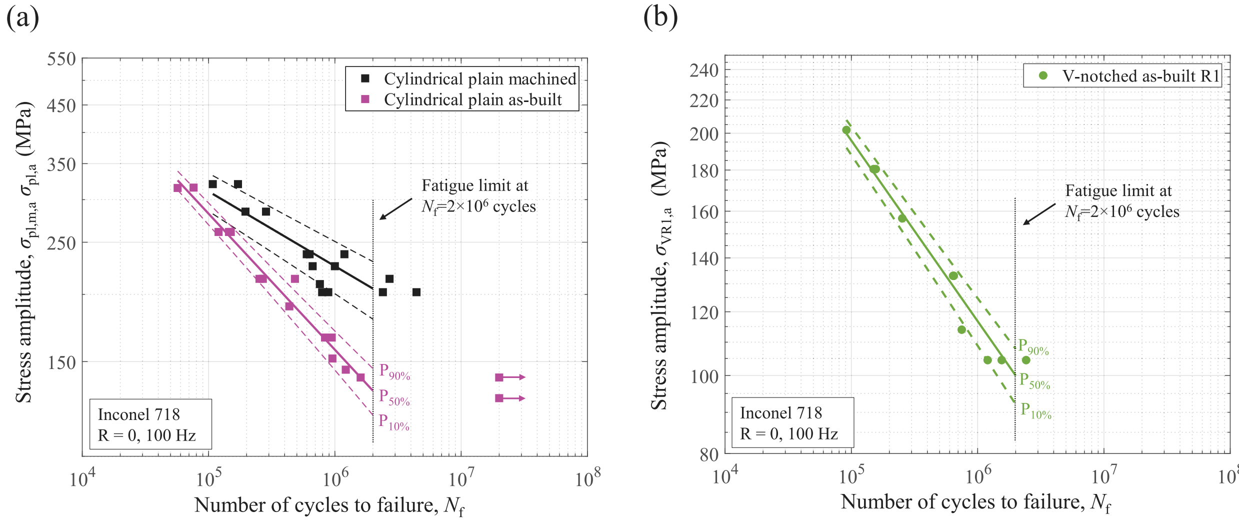

Fig. 5. SN curves of (a) the plain machined and as-built specimens and (b) of the VR1 as-built specimens.

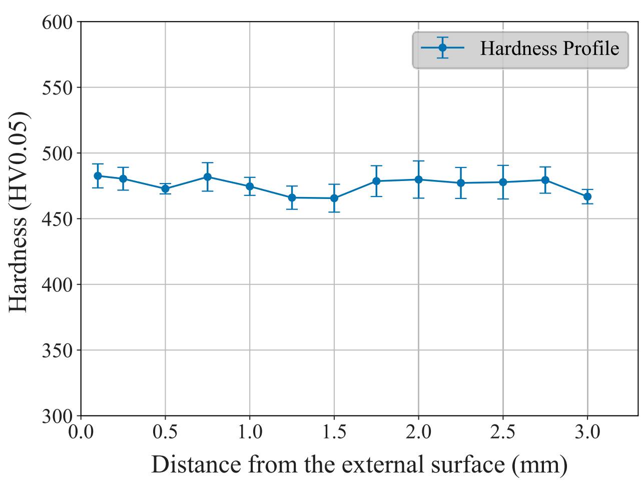

Fig. 6. Performed hardness measurements.

2.3. Fractographic analyses

Fractographic analyses were necessary to understand the fatigue crack initiation locations and the causes of failure for the different specimens, thus several inspections were performed with the SEM. The obtained results are shown in Fig. 7. Fig. 7(a) represents an example of the crack initiation mechanism for a VR02 specimen, and, due to severity of the notch, the fatigue failure of these samples was triggered by the notch. In the other specimens (VR1 and plain both as-built and machined) the situation was a bit different. As concerns the VR1 machined and the plain machined specimens represented in Figs. 7(b) and (c), respectively, the pores played a crucial role in the crack initiation, and, in the VR1 machined specimens a combination of the notch and the pores led to failure, while in the plain machined specimen the combination between the surface roughness and the pores led to failure. In the plain as-built and the VR1 as-built specimens, represented in Figs. 7(d) and (e), respectively, a cooperation between the pores and the surface roughness, for the plain as-built, and between the pores, the surface roughness and the notch, for the VR1 as-built, triggered the fatigue crack initiation.

2.4. Microstructural analysis

The optical microscope (OM) and the SEM were employed to investigate the grains size and orientation. The specimens were prepared according to ASTM E3-11 standard and were subjected to etching using Kalling's II (n.94, ASTM E407) and the results are shown in Fig. 8. In Figs. 8(a) and (b) the analyses of a longitudinal section are shown, while in Figs. 8(c) and (d) the analyses of a transversal section are presented, and, as shown in Figs. 8(a) and (b), it was obtained that the grains are elongated along the BD. In Fig. 8 some of the grains are contoured in white. Grain size was measured according to ASTM E112 using the line-intercept method. This included an overall count of about 50 grains on both cross sections. The obtained grain size numbers were G = 2.10 in the longitudinal direction and G = 6.47 in the transversal direction, corresponding to 171 μm and 38 μm, respectively. Finally, the aspect ratio of the grains was calculated as $A_{r,g} = 38/171 = 0.22$. Given that the specimens were produced in the same batch and with the same production parameters (laser power, scan velocity, hatch distance, layer thickness, meltpool aspect ratio, energy density and LPBF build rate), the same grain shape and grain aspect-ratio were obtained near the external surface and in the bulk zone, thus confirming the homogeneity of the obtained specimens.

To investigate the effect of pores on the fatigue strength, OM analyses were necessary to understand the shape, the size and the distance from the external surface of the pores. As concerns the plain specimens, four as-built samples were prepared with four cross-sections for each specimen. A 500 μm thick layer was removed from each cross-section with mechanical polishing of each sample. An example of the results obtained for the plain specimen is shown in Fig. 9(a), where it is highlighted the sporadic presence of pores, which were mostly located near the external surface thus their detrimental effect interacted with that provided by the surface roughness. The distance of the pores from the external surface was a significant quantity in this research, and it was defined as the lowest distance from the external surface to the pore as shown in Fig. 9(b), and this definition was applied for both plain and V-notched specimens. The internal pores in both the blunt V-notched and the plain specimens were considered spherical in the FE modelling explained below, and this is due to the thermodynamics nature of the internal pores given that they are obtained from entrapped gas bubbles according to our previous research Ref. [46]. In addition to this, in Ref. [46] an investigation on the pores aspect ratio, defined as the ratio between the two major perpendicular axes, was performed in specimens obtained with the same 3D printed parameters and aging process as those of this research, and a value close to 1 was obtained. The almost

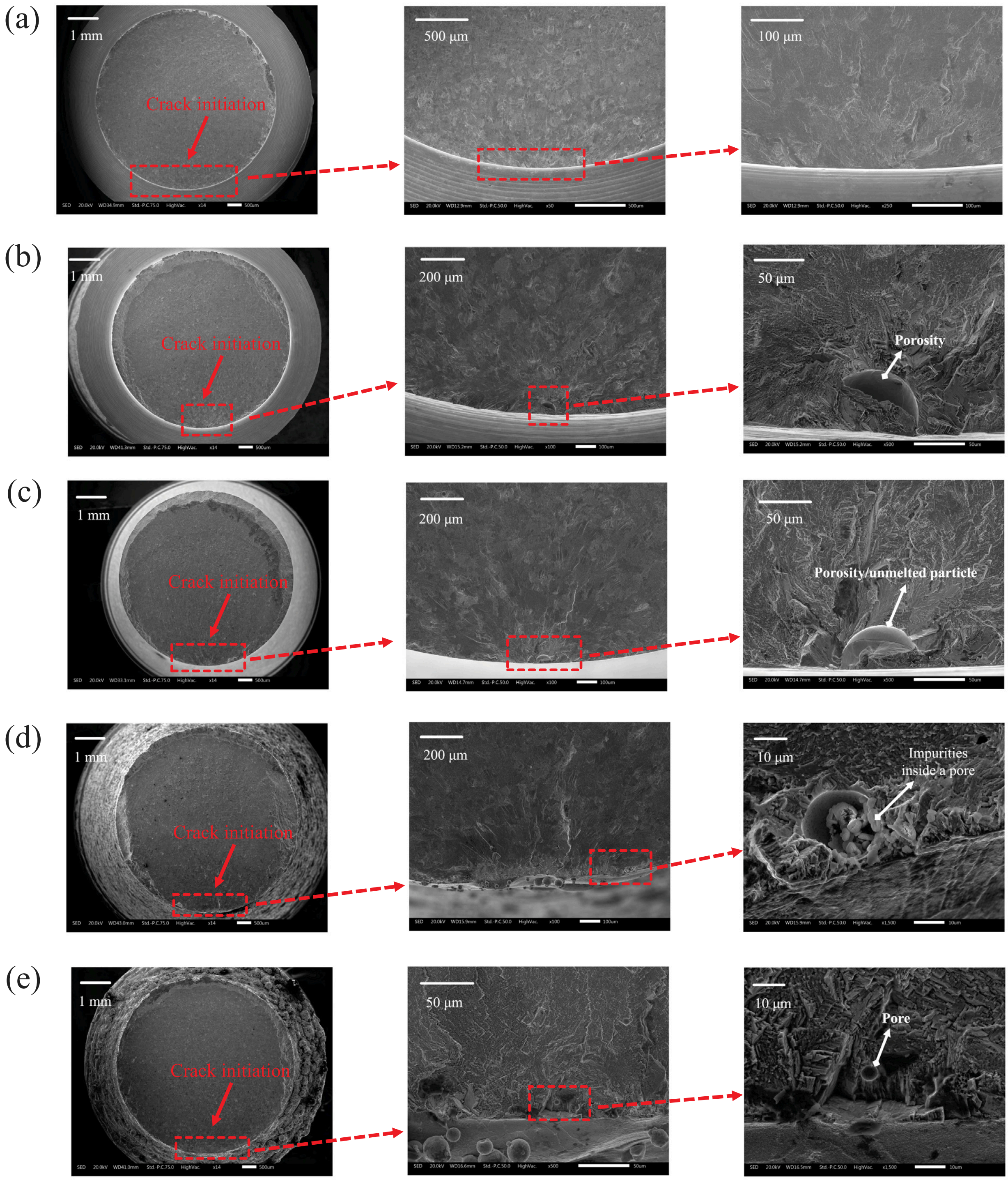

Fig. 7. Fractographic analyses with SEM of the broken specimens: (a) VR02, (b) VR1 machined, (c) plain machined, (d) plain as-built and (e) VR1 as-built.

spherical shape of the pores was also confirmed in Fig. 9(a). Finally, the precipitates in the samples were analysed with the SEM. The samples were characterized by the presence of plate-like precipitates at the grain boundaries, along with a homogeneous distribution of much finer particles within the grains. These finer particles exhibit two different morphologies: cubic and needle-like. According to literature data, the precipitates at the grain boundaries are δ-Ni3Nb, while within the grains there are cubic γ'-Ni3Al (Ni3Ti) and plate-like γ''-Ni3Nb, as indicated in Fig. 9(c). Some globular metal carbides (MC) were also observed as shown in Fig. 9(c). The obtained results concerning the precipitates are coherent with that found in Refs. [5,69–74]. In fact, TTT diagrams and microstructural investigations reveal the presence of these precipitates in conventionally heat-treated Inconel 718. Pore investigations were also implemented for the machined VR1 specimens where the cross-sections of 10 specimens near the notch were analysed. The obtained 2D images were captured using a DSX1000 digital microscope, and the defect detection was performed using ImageJ software. An example of the obtained results is shown in Fig. 10(a), and the pores were still sporadic and mostly located next to the external surface. The pores shape obtained in the machined VR1 specimens was still almost spherical, and the observed precipitates were the same as those obtained in the plain specimens as shown in Fig. 10(b).

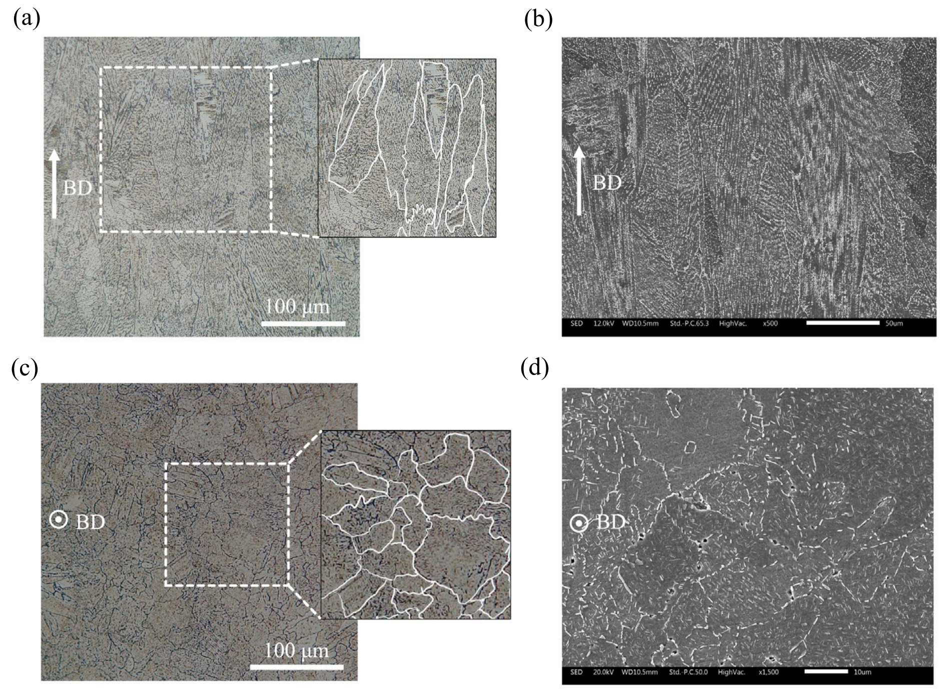

Fig. 8. Grains analysis of the specimens: (a) longitudinal section analysed with OM, (b) longitudinal section analysed with SEM, (c) transversal section analysed with OM and (d) transversal section analysed with SEM.

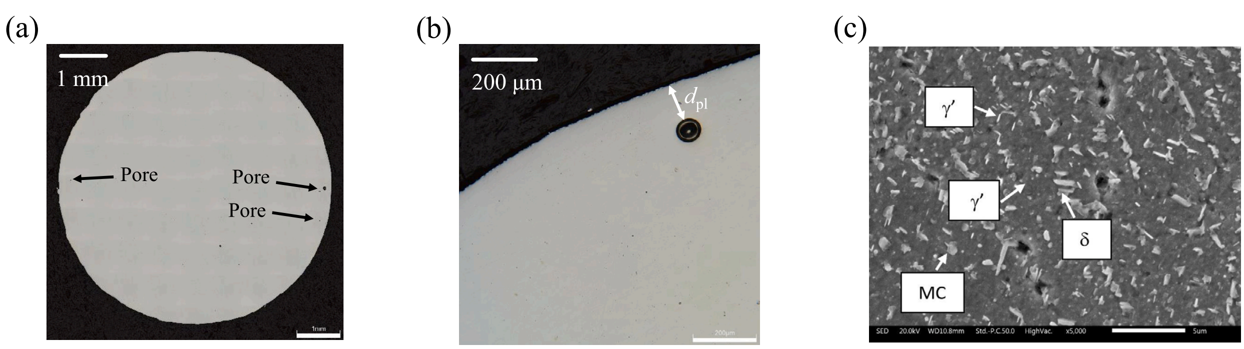

Fig. 9. Microstructural analysis of the as-built plain specimens: (a) transversal cross section showing internal pores, (b) definition of the distance of the pore from the external surface and (c) SEM showing the distribution of the precipitates.

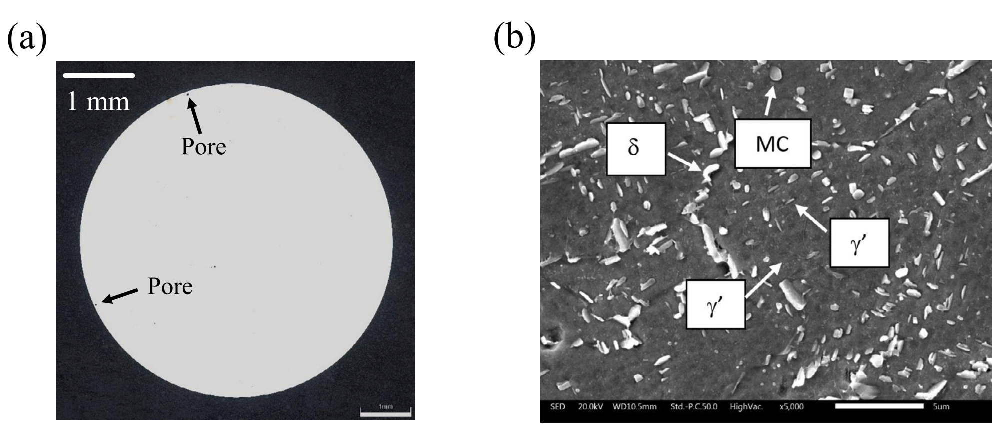

Fig. 10. Microstructural analysis of the machined VR1 specimens: (a) transversal cross section showing internal pores, (b) SEM showing the distribution of the precipitates.

From each scanned surface, both for the plain and the VR1 specimens, the maximum diameter of the pore ($D_{\mathrm{pl,max}}$ for the plain specimens and $D_{\mathrm{N,max}}$ for the VR1 specimens) and the corresponding distance from the external surfaces (d_{pl} for the plain specimens and d_{N} for the VR1 specimens) were extracted. The relationship between these latter quantities was investigated with the Pearson correlation factor r [75], which is described in Eq. (4) for two random variables x and y. In Eq. (4) the quantites μ_x and μ_y represent the sample averages of x and y, respectively, while N represents the number of experimental data. The coefficient r is ranged from -1 to 1, and two quantities can be considered correlated if the coefficient is near to -1 or 1, while they are weakly correlated if the coefficient is near 0. In our case, the quantities x and y were the maximum pore diameter and the corresponding distance from the external surface, and we obtained that $|r| < 0.5$ for the plain and the VR1 specimens. However, the Pearson correlation factor should be strictly used when the distribution of two variables is normal and they are linked by a linear relationship, otherwise the Spearman [76] and the Kendall [77] correlation factors must be employed. To calculate the Spearman correlation factor between two random variables x and y, they must be firstly transformed into the corresponding ranks $\mathrm{R}[x]$ and $\mathrm{R}[y]$. For example, if the first value of x corresponds to the smallest among all the values of x, we have that $\mathrm{R}[x_1] = 1$, and this reasoning can be applied to the y variable too. Once $\mathrm{R}[x]$ and $\mathrm{R}[y]$ are obtained, the Spearman correlation factor r_{s} can be calculated according to Eq. (5). The Kendall correlation factor is described in Eq. (6) where x and y represent the random variables and N represents the number of experimental data. The computation of the Kendall and the Spearman correlation factors gave low values, and $|r_{\mathrm{s}}, r_{\mathrm{k}}| < 0.5$. Finally, the obtained low correlation factors did not justify a clear correlation between the two quantities, thus the distribution functions of the pore diameters and the distances from the external surface were analysed separately both for the plain and the VR1 specimens. As-concerns the statistical analysis of the pore diameters in the plain specimens, the applied approach took inspiration from Ref. [42], and an extreme value statistical approach, in this case the distribution function of Gumbel described in Eq. (7), was employed. In Eq. (7), a and b are two unknown parameters to be tuned, and the values of the cumulative probability F_{G} were calculated consistently with the Murakami approach presented in Ref. [42] where, given i the index of a pore diameter among N measured values sorted in an ascending order, $F_{\mathrm{G},i} = i/(N+1)$ i.e. the value that the sampling distribution assumes for the i−th value of the sample of the random variable. This latter definition of the cumulative probability was extended to all the other distribution functions employed in this research. The parameters a and b were obtained with the least squares method with a confidence interval of 80%. The experimental data with the fitted distribution function of Gumbel are shown in Fig. 11(a) where the envelope curves, represented with blu dashed lines, have been obtained with the parameters at the upper and lower bounds of the chosen confidence interval. For each cross-section, the pore with the maximum diameter was recorded and its distance from the external surface was also considered a quantity of interest for this research, however, there is not a clear indication in the literature about the distribution function to be used in modelling the distance of the pores from the external surface. For example in Ref. [78] it is suggested that the defect location can be assumed uniformly distributed in the specimen, while in Ref. [79] the pore distribution was modelled with a log-normal distribution function. In this research, the Kolmogorov–Smirnov test was implemented to identify a distribution function suitable to model the distance of the pores from the external surfaces, and it was obtained that the null hypothesis, which supposed that the experimental data comes from the chosen probability distribution, was not refused with a p-value = 0.83 for the exponential distribution function. The obtained results from the Kolmogorov–Smirnov test did not assure that this distribution function is correct, however, the obtained p-value was high. The exponential distribution function is described in Eq. (8) where μ is the unknown parameter to be calculated. The experimental data of the distance of the pores from the external surface in the plain specimens are shown in Fig. 11(b) together with the fitted exponential distribution function whose parameter was obtained with a confidence interval of 80% and with the least squares method. The dashed blu lines in Fig. 11(b) represent the envelope of the curves obtained with the parameter at the upper and lower bounds of the chosen confidence interval. The above mentioned distribution functions (Gumbel and exponential) of the pore diameters and the distance from the external surface were used for the plain specimens both as-built and machined. It might be argued that there could be some differences, concerning the pores, between the plain machined and the plain as-built specimens due to the turning machining operation performed in the machined specimens to reduce the surface roughness, however, the turning machining operation generally takes one or two tenth of millimeter, thus with a low impact on the pores distribution. In fact, the turning machining operation has a low impact on the internal porosity of AM components, and, as shown by Chen et al. in Ref. [80], the hot isostatic pressing should be employed to reduce the presence of internal pores. The obtained parameters of Eqs. (7) and (8) together with their confidence intervals are reported in Table 5.

$$r = \frac{\sum_{i=1}^{N}\left(x_i-\mu_x\right)\left(y_i-\mu_y\right)}{\sqrt{\sum_{i=1}^{N}\left(x_i-\mu_x\right)^2}\sqrt{\sum_{i=1}^{N}\left(y_i-\mu_y\right)^2}} \tag{4}$$

$$r_{\mathrm{s}} = \frac{\operatorname{cov}\left(\mathrm{R}[x],\mathrm{R}[y]\right)}{\sigma_{\mathrm{R}[x]}\sigma_{\mathrm{R}[y]}} \tag{5}$$

$$r_{\mathrm{k}} = \frac{2}{N(N-1)}\sum_{i=1}^{N-1}\sum_{j=i+1}^{N}\operatorname{sgn}\left(x_i-x_j\right)\operatorname{sgn}\left(y_i-y_j\right) \tag{6}$$

$$F_{\mathrm{G}} = e^{-e^{\left(-\frac{D_{\mathrm{pl,max}}-b}{a}\right)}} \tag{7}$$

$$F_{\mathrm{E}} = e^{\left(1-\frac{d_{\mathrm{pl}}}{\mu}\right)} \tag{8}$$

The approach implemented for the plain specimens was also adopted for the pores in the VR1 specimens. Also in this case from each cross section the pore with the maximum diameter was identified, and, in this case, the generalized extreme value distribution function was found appropriate given that it was able to capture the initial "tail" of the experimental data shown in Fig. 12(a). The Kolmogorov–Smirnov test was employed and the null hypothesis was not refused with a p-value = 0.99. The generalized extreme value distribution function is described in Eq. (9) where ζ, μ_{gev} and σ_{gev} are the unknown parameters to be computed. The term ζ represents the shape parameter, and for values of ζ near to 0, the generalized extreme value distribution function returns the distribution function of Gumbel. The experimental data and the fitted curve are reported in Fig. 12(a), and the unknown parameters were obtained with the least squares method. In Fig. 12(a) the dashed blue lines represent the envelope of the curves obtained with the parameters at the upper and lower bounds of the chosen confidence interval. As in the plain specimen, the distance from the external surface of the pore with the maximum diameter in each cross section was statistically significant also in the VR1 specimens. The generalized extreme value distribution function was still found appropriate, and it was obtained that the null hypothesis was not refused with p-value = 0.78. The experimental data with the fitted curve are shown in Fig. 12(b), and the dashed blue lines still represent the envelope of the curves obtained with the parameters at the upper and lower bounds of the chosen confidence interval. Also in this case it was assumed that the turning machining operation did not considerably affect the pores distribution in the V-notched specimens, thus the same distribution functions were assumed valid both for the VR1 machined and as-built specimens. The obtained parameters of Eq. (9) together with their corresponding confidence interval of 80% are reported in Table 6.

$$F_{\mathrm{V}} = e^{-\left(1+\zeta\frac{D_{\mathrm{N}}-\mu_{\mathrm{gev}}}{\sigma_{\mathrm{gev}}}\right)^{-\frac{1}{\zeta}}} \tag{9}$$

Table 5
Numerical values obtained for the parameters of the Gumbel and exponential distribution functions concerning the pores of the plain specimens.

Quantity	Pore diameter	Distance from the external surface
Parameter 1	$a = 14.5$ μm	$\mu = 411$ μm
Parameter 2	$b = 45.9$ μm	/
Confidence interval parameter 1	$(13.7 \leq a \leq 15.3)$ μm	$(381 \leq \mu \leq 441)$ μm
Confidence interval parameter 2	$(45.0 \leq b \leq 46.8)$ μm	/

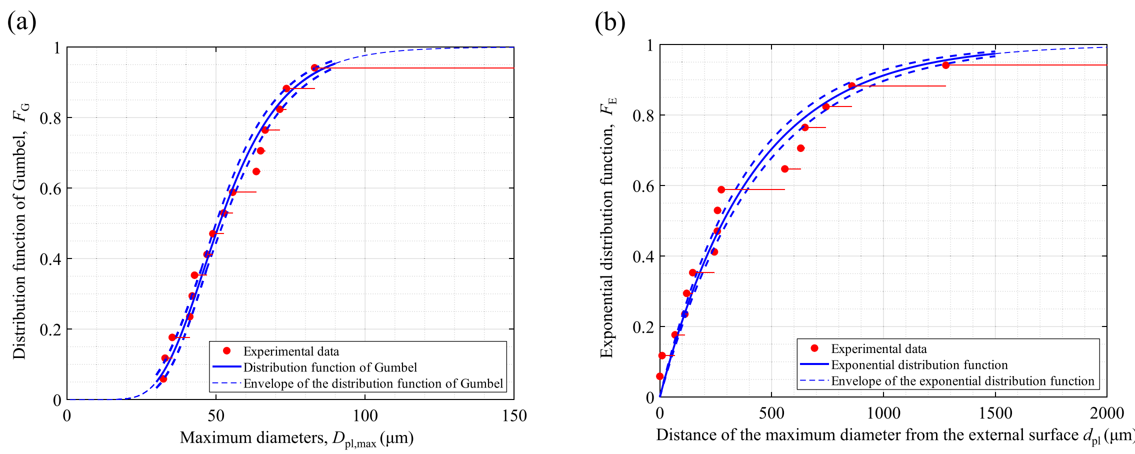

Fig. 11. Statistical analysis of the pores in the plain specimens: (a) distribution function of Gumbel to model the pore diameter and (b) exponential distribution function to model the distance from the external surface.

Table 6
Numerical values of the parameters obtained for the generalized extreme value distribution functions concerning the pores of the V-notched specimen.

Quantity	Pore diameter	Distance from the external surface
Parameter 1 (μ_{gev})	41.8 μm	67.1 μm
Parameter 2 (σ_{gev})	25.0 μm	59.6 μm
Parameter 3 (ζ)	0.482	1.26
Confidence interval parameter 1	$(39.3 \leq \mu_{gev} \leq 44.3)$ μm	$(58.6 \leq \mu_{gev} \leq 75.6)$ μm
Confidence interval parameter 2	$(20.7 \leq \sigma_{gev} \leq 29.2)$ μm	$(40.9 \leq \sigma_{gev} \leq 78.3)$ μm
Confidence interval parameter 3	$0.169 \leq \zeta \leq 0.795$	$0.678 \leq \zeta \leq 1.85$

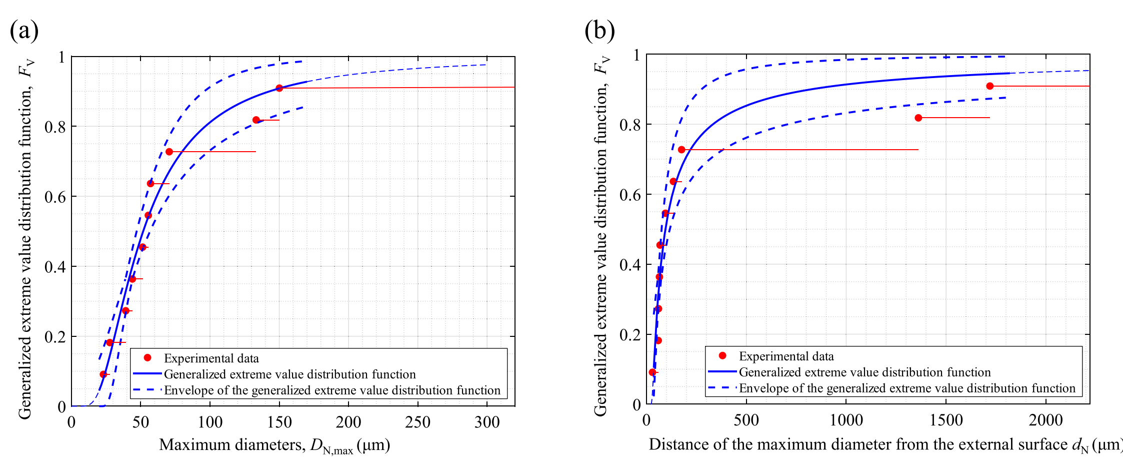

Fig. 12. Statistical analysis of the pores in the VR1 specimens: generalized extreme value distribution function to model (a) the pore diameter and (b) the distance from the external surface.

2.5. Optical profilometer observations

The surface morphology was analysed with the optical profilometer Taylor Hobson CCI MP-L, which makes use of the coherence correlation interferometry, which means that a light source is divided in two paths, one moves to the reference surface while the other moves to the test surface. The two reflected rays of light finally combine at a camera detector, and their interference fringes reproduce the surface morphology. Given that the effect of the surface roughness was detrimental for the fatigue strength of the plain and VR1 as-built specimens and it also had an influence on the fatigue strength of the plain machined specimens, the scans were performed on as-built and machined plain specimens and on the VR1 as-built specimens. Some of the obtained results are shown in Fig. 13. In Figs. 13(a) and (b) two examples of the scans obtained from the plain as-built and machined specimens, respectively, are shown. In the plain specimens the surface investigations focused on the central zone, which, accordingly to our previous research Ref. [65], was the highly stressed surface. In addition, it is possible to observe the differences between the surface topographies of the as-built plain specimen of Fig. 13(a) and the machined plain specimen of Fig. 13(b). In Fig. 13(c) the result of one of the scans performed on the VR1 as-built specimen is reported, and in this case the analysis was focused on the zone around the notch, which is the most critical part of the specimen. Fig. 13(d) shows the optical profilometer while scanning the VR1 as-built specimen around the notch.

3. Fatigue strength analyses

3.1. Determination of the critical distances

In Ref. [39] a procedure to calculate the critical distances L and L' according to the line and point methods, respectively, and for mode I loading case was proposed. The above mentioned procedure was based on the combination of a plain specimen and a sharp V-notched specimen with the aim of overcoming the determination of the quantity ΔK_{th}, which was employed in the classical determination of the critical distance according to the El-Haddad formulation proposed in Ref. [81]. The determination of the quantity ΔK_{th} can be, in fact, a challenging task as highlighted in Ref. [82]. The procedure proposed in Ref. [39] stands that the critical distance, for both the line and point methods, is a function of the ratio between the sharp V-notched specimen radius R_N and $D/2$, where D is the bar diameter, i.e. the gros diameter of the V-notched specimen, and of the ratio between σ_a^* or $\sigma_a^{*'}$ and $\sigma_{VR02,m,a}$ where σ_a^* and $\sigma_a^{*'}$ are the intrinsic fatigue strength values according to LM and PM, respectively, and $\sigma_{VR02,m,a}$ is the fatigue strength of the machined sharp V-notched specimen. In this case the sharp V-notched specimen had a nominal notch radius equal to $R_N = 0.2$ mm, and, in principle, the intrinsic fatigue strength should coincide with the fatigue strength of the machined plain specimen, thus the critical distances could be obtained with Eqs. (10) and (11) for LM and PM, respectively.

$$L = \frac{D}{2}\, f\left(\frac{R_{02}}{D/2}, \frac{\sigma_a^*}{\sigma_{VR02,m,a}}\right) \tag{10}$$

$$L' = \frac{D}{2}\, g\left(\frac{R_{02}}{D/2}, \frac{\sigma_a^{*'}}{\sigma_{VR02,m,a}}\right) \tag{11}$$

According to Fig. 7(c), the plain machined specimens had some pores near the external surface which triggered the crack initiation, thus the intrinsic fatigue strength was not considered equal to that of the machined plain specimen. This case was the same as that of Ref. [54] for cast iron specimens, and it can be solved by combining the two V-notched specimens, i.e. the machined sharp V-notched specimen and the machined blunt V-notched specimen ($R_N = 1$ mm). This latter procedure is described in Eqs. (12) and (13), where $\sigma_{VR1,m,a}$ is the fatigue strength of the machined blunt V-notched specimen, R_1 and R_{02} are the notch radii of the blunt and sharp V-notched specimens, and D_1 and D_{02} are the bar diameters of the blunt and the sharp V-notched specimens. In principle the bar diameters of the V-notched specimens are equal according to Figs. 3(a) and (b), however, once printed, these two values can present differences, which are of fundamental importance for an accurate determination of the critical distances. For this reasons, the diameters D_{02} and D_1 were measured, and it was obtained that D_{02}=8.67 mm, and $D_1 = 8.63$ mm. Besides this, the values of the notch radii were measured after an analysis with the SEM, and the values of $R_1 = 930$ μm and $R_{02} = 184$ μm were obtained. The only unknown quantities in Eq. (12) were the intrinsic fatigue strength values σ_a^* and $\sigma_a^{*'}$, which were determined after some iterations with the MATLAB script proposed in the appendix of Ref. [39].

$$\frac{D_{02}}{2}\, f\left(\frac{R_{02}}{D_{02}/2}, \frac{\sigma_a^*}{\sigma_{VR02,m,a}}\right) = \frac{D_1}{2}\, f\left(\frac{R_1}{D_1/2}, \frac{\sigma_a^*}{\sigma_{VR1,m,a}}\right) \tag{12}$$

$$\frac{D_{02}}{2}\, g\left(\frac{R_{02}}{D_{02}/2}, \frac{\sigma_a^{*'}}{\sigma_{VR02,m,a}}\right) = \frac{D_1}{2}\, g\left(\frac{R_1}{D_1/2}, \frac{\sigma_a^{*'}}{\sigma_{VR1,m,a}}\right) \tag{13}$$

The use of the double notch inversion to obtain the values of the critical distances assumed that the notch triggers the fatigue crack, and this was confirmed in Fig. 7(a) for the machined VR02 specimen. However, as shown in Figs. 4 and 7(b), a combination between the notch and a pore near the external surface could be responsible for the fatigue failure of the machined VR1 specimen. For this reason at the FL (2×10^6 number of cycles), the specimen indicated with 1 in Fig. 4 was used to calculate the critical distances. In fact, as shown in Fig. 4, the fatigue failure of this specimen was only driven by the notch given that no pores were detected next to the crack initiation zone, and, for this reason, it was called intrinsic machined VR1 specimen. The chosen fatigue strength value of the machined VR1 specimen to perform the determination of the critical distance at 2×10^6 number of cycles was equal to $\sigma_{VR1,m,a} = 190$ MPa, and it was then employed in Eqs. (12) and (13). Once the values of σ_a^* and $\sigma_a^{*'}$ were obtained, the corresponding values of the critical distances were calculated according to Eqs. (14) and (15), and it was obtained that $L = 13.7$ μm and $L' = 24.7$ μm at 2×10^6 number of cycles.

$$L = \frac{D_{02}}{2}\, f\left(\frac{R_{02}}{D_{02}/2}, \frac{\sigma_a^*}{\sigma_{VR02,m,a}}\right) \tag{14}$$

$$L' = \frac{D_{02}}{2}\, g\left(\frac{R_{02}}{D_{02}/2}, \frac{\sigma_a^{*'}}{\sigma_{VR02,m,a}}\right) \tag{15}$$

Given that the only available fatigue strength value for the intrinsic machined VR1 specimen was at 2×10^6 cycles, in principle we could not obtain the values of the critical distances at lower number of cycles to failure. Strictly speaking, the fatigue strength predictions could only be obtained at the FL. In Ref. [83] it is highlighted that the influence of the notch in fatigue failure can become negligible at low numbers of cycles to failure, thus the fatigue strength of a notched specimen is similar to the fatigue strength of a plain (unnotched) specimen. This latter because at low numbers of cycles to failure the plasticity plays a fundamental role in redistributing the stresses. For example, in Fig. 5 it is shown that the difference between the fatigue strength of the machined VR02 and VR1 specimens decreases at low number of cycles to failure. Generally, the number of cycles to failure to consider the fatigue strength of a notched specimen equal to that of the corresponding plain specimen can be fixed at 10^3 according to Ref. [83]. For this latter reason the curve of the intrinsic machined VR1 specimen was supposed to intersect the fatigue curve of the experimental machined VR1 specimen at 10^3 number of cycles. The fatigue curve of the intrinsic machined VR1 specimen was then obtained by supposing that the point, in terms of number of cycles to failure and stress amplitude, (2×10^6;190) satisfies the Basquin equation and that the fatigue curves of the intrinsic machined VR1 specimen and the machined VR1 specimen intersect each other at 10^3 number of cycles to failure. The obtained curve of the intrinsic machined VR1 specimen is then shown in Fig. 14. The obtained Basquin curves of the machined VR02 specimen and of the intrinsic machined VR1 specimen were employed, according to the procedure proposed by Santus et al. in Ref. [39] and described in Eqs. (12), (13), (14) and (15), to calculate the values of the critical distances L and L' at the experimental numbers of cycles to failure, below the FL, of the as-built plain specimens, and the obtained results are shown in Fig. 15(a). The obtained values of the critical distances by varying the number of cycles to failure were fitted with the curves described in Eqs. (16) and (17). These latter equations provide a dependence of the critical distance on the number of cycles to failure described by an exponential relationship with the parameters A, B, A_1 and B_1 which was proposed by Susmel and Taylor in Ref. [84]. The obtained values of the parameters of Eq. (16) are $A = 24.0$ μm and $B = -0.039$, while $A_1 = 45.1$ μm and $B_1 = -0.041$ are obtained for the parameters of (17). Given that, as shown in Fig. 15(a), Eqs. (16) and

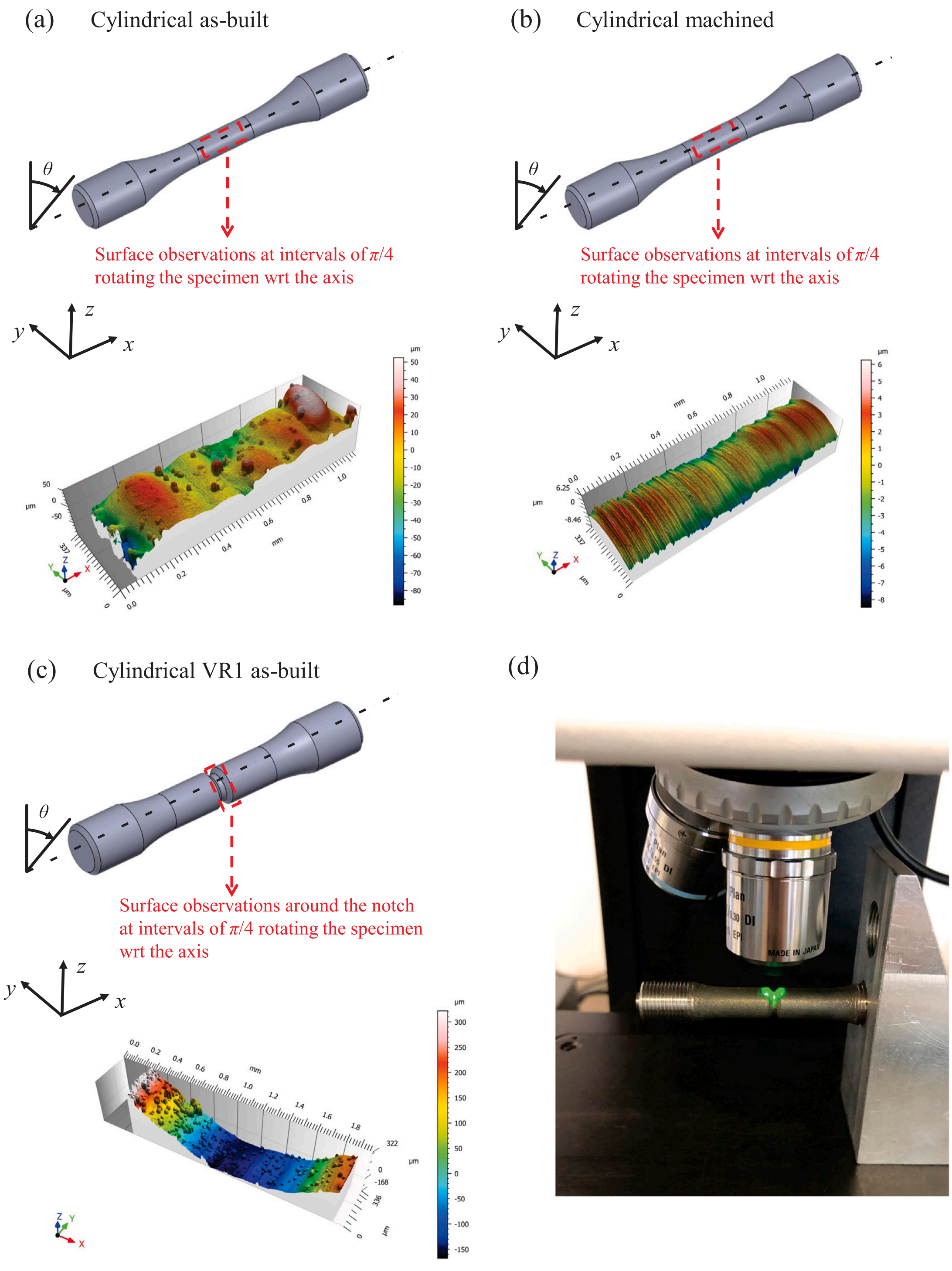

Fig. 13. Examples of scans performed on (a) the plain as-built specimen, (b) the plain machined specimen, (c) the VR1 as-built specimen and (d) optical profilometer during scanning operation of the VR1 as-built specimen.

(17) can well represent the dependence of the critical distance on the number of cycles to failure, the obtained curves were then employed to calculate the values of L and L' in correspondence of the experimental numbers of cycles to failure of the plain machined, the as-built VR1 and the machined VR1 specimens. The values of the fatigue strength of the intrinsic plain specimen σ_a^* and $\sigma_a^{*\prime}$ were calculated for the plain as-built specimens by varying the number of cycles to failure, and they are reported in Fig. 15(b). According to the procedure proposed in Ref. [39], the obtained intrinsic fatigue strength data can be perfectly

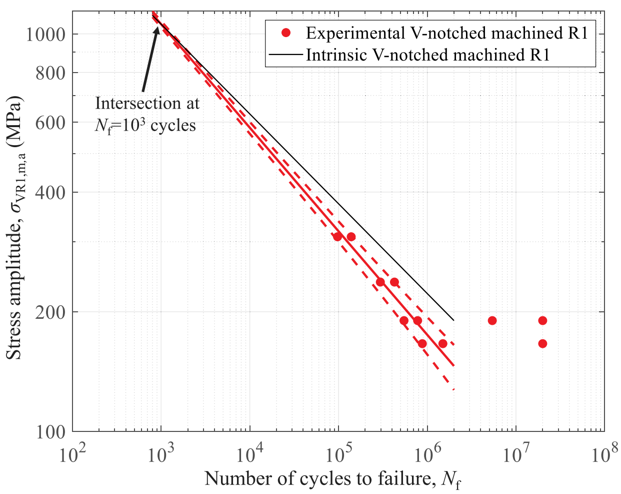

Fig. 14. SN curves of the machined VR1 specimen and of the intrinsic machined VR1 specimen.

fitted with a Basquin curve (Eq. (2)) as described in Fig. 15(b).

$$L = A\left(N_f\right)^B \tag{16}$$

$$L' = A_1\left(N_f\right)^{B_1} \tag{17}$$

3.2. FE analyses

In all the FE models an isotropic linear elastic constitutive behaviour of the material was introduced through the quantities E and ν. The Young modulus E was the same as that of Table 3, while the Poisson Ratio, as mentioned in 2.2, was taken from Barros et al. in Ref. [67]. Some of the surface profile scans obtained with the optical profilometer were modelled with FEM. Plane axisymmetric 182 elements were employed for FE modelling as shown in Figs. 16(a), (b) and (c) for the plain as-built, the plain machined and the VR1 as-built specimens, and the submodelling technique was implemented focusing on the zone close to the scanned profile. A unitary stress was applied at the top of the model for the plain as-built and machined specimens, while in the machined VR1 specimen the stress applied at the top of the model was obtained by considering an applied unitary stress in the net section, thus the minimum section of the specimen, which was scaled by the quadratic ratio between the diameters of the net (6 mm) and the gros (8.63 mm) sections. After FE simulations, the axial stress σ_x was extracted along the radial paths starting from the surface profile valleys where a stress concentration was expected. The theory of critical distances according to LM and PM was applied to calculate the FSCFs $K_{f,rough}$ and $K'_{f,rough}$ provided by the surface roughness as described in Eqs. (18) and (19). In these latter equations L and L' are the critical distances obtained with LM and PM, respectively, with the procedure presented in 3. In order to make a statistical analysis of the FSCFs, one hundred values of $K_{f,rough}$ and $K'_{f,rough}$ were obtained, and they were fitted with an extreme value distribution function (Gumbel in this case), which was found appropriate to model the distribution of the stress concentration factors according to Refs. [55,85]. The experimental data together with the fitted curve are reported in Fig. 17 for the FSCFs obtained with the LM at the FL, and the parameters of the Gumbel curves were obtained with a confidence interval of 80%. In Fig. 17 the dashed blue lines represent the envelope of the curves obtained with the parameters at the upper and lower bounds of the chosen confidence interval. The obtained values of the Gumbel parameters a and b with the confidence intervals of 80% are reported in Table 7 for both the LM and the PM. The values corresponding to 99% of probability were calculated, and they were then employed in the fatigue strength prediction calculations which are better explained below. The FSCFs obtained with FE simulations of the as-built VR1 specimen, which are shown in Fig. 17(c), correspond to the combination between the stress concentration effect provided by the surface roughness and the notch.

$$K_{f,rough} = \frac{1}{2L}\int_0^{2L} \sigma_x \mathrm{d}y \tag{18}$$

$$K'_{f,rough} = \sigma_x\left(\frac{L'}{2}\right) \tag{19}$$

The FE modelling of the pores was based on the distribution functions obtained to describe the pore diameters and the corresponding distances from the external surfaces (Eqs. (7), (8) and (9) for the plain and the VR1 specimens). By reversing the obtained expressions, the relationships between the pore diameters ($D_{pl,max}$ and $D_{N,max}$) or the distances from the external surfaces (d_{pl} and d_n) and F_G or F_V or F_E were obtained. After this, one hundred values of F_G and F_V were generated according to an uniform distribution function, and then one hundred values of pore diameters were calculated. Finally, one hundred values of F_E and F_V were generated again, and one hundred values of the distances from the external surface were obtained. It is important to highlight that the one hundred values of pore diameters and distances from the external surfaces were calculated separately because of the low correlation between the two variables as demonstrated in 2.4. The obtained one hundred samples of pore diameters and distances from the external surfaces were used in FE simulations, which are shown in Fig. 18. In the FE models of the pores, 3D elements were used as shown in Fig. 18, and only one spherical pore was included. This latter aspect can be motivated by observing Figs. 9(a) and 10(a), where the distances between the observed pores is much higher than the values of the critical distances, thus a low interaction between different pores was supposed. In the plain specimen, once the simulation was performed, various points on the external surface of the pore were selected as starting points of the radial paths to calculate the FSCFs $K_{f,pore}$ and $K'_{f,pore}$ according to LM and PM, respectively. After FE simulations, the axial stress σ_x was evaluated along the radial path, and it was employed to calculate the values of $K_{f,pore}$ and $K'_{f,pore}$ by using the same expressions as Eqs. (18) and (19). The highest obtained values of $K_{f,pl,pore}$ and $K'_{f,pl,pore}$ for the simulated pore were selected and the same operations were repeated for all the other pores. In FE simulations of the pores of VR1 specimen, the aim was to obtain the impact of the pores on the FSCFs provided by the notch, which were defined as $K_{f,N}$ according to LM and $K'_{f,N}$ according to PM. To accomplish this, an initial FE model of the blunt V-notched specimen was implemented and the corresponding FSCFs $K_{f,N}$ and $K'_{f,N}$ were calculated according to TCD. After this, 3D FE simulations of the notched geometry with a spherical pore were performed as shown in Fig. 18(b) and the axial stress σ_x was evaluated along the radial path with the starting point corresponding to point A. The FSCFs $K_{f,VR1,pore}$ and $K'_{f,VR1,pore}$ according to LM and PM, respectively, were then calculated with Eqs. (20) and (21). This procedure to calculate the effect of the pore on the fatigue strength of the VR1 specimens can be motivated by observing Fig. 4. In this latter it is highlighted that a combination between the pore and the notch triggered the fatigue crack initiation of the majority of the VR1 machined specimens, except for that indicated with 1, which failed at $\sigma_{VR1,m,a}$ = 190 MPa. This latter value was then chosen as the FL of the intrinsic VR1 machined specimen. The difference between the fatigue strength of the specimen indicated with 1 in Fig. 4 and the FL obtained by fitting the Basquin curve on the experimental data of the machined VR1 specimen (red curve in Fig. 4) should be explained by considering the additional effect of the pore. This latter aspect will be better clarified below. The obtained FSCFs provided by the pores were then fitted with an extreme value distribution function, and in particular the distribution function of Gumbel was found appropriate to

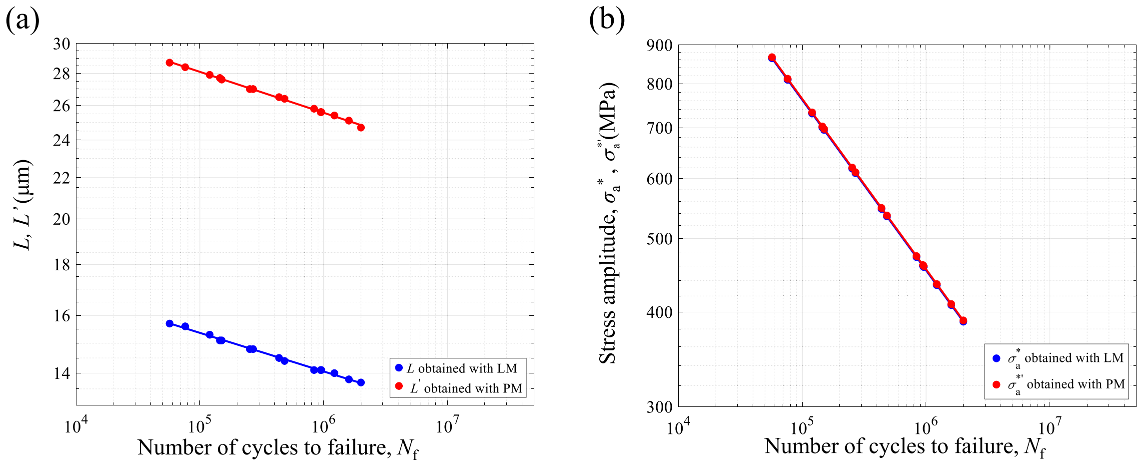

Fig. 15. (a) Critical distance values versus the number of cycles to failure and (b) intrinsic fatigue strength versus the number of cycles to failure.

Table 7
Numerical values obtained for the parameters of the distribution function of Gumbel concerning the FSCFs, calculated with LM and PM, at the FL provided by the surface roughness in the as-built blunt V-notched specimen and the as-built and machined plain specimens.

Quantity	As-built blunt V-notched	As-built plain	Machined plain
Parameter 1 (LM)	$a = 0.230$	$a = 0.116$	$a = 0.0239$
Parameter 2 (LM)	$b = 2.281$	$b = 1.193$	$b = 1.218$
Confidence interval parameter 1 (LM)	$(0.228 \le a \le 0.233)$	$(0.114 \le a \le 0.118)$	$(0.0234 \le a \le 0.0244)$
Confidence interval parameter 2 (LM)	$(2.277 \le b \le 2.284)$	$(1.190 \le b \le 1.195)$	$(1.217 \le b \le 1.219)$
Parameter 1 (PM)	$a = 0.214$	$a = 0.101$	$a = 0.0162$
Parameter 2 (PM)	$b = 2.115$	$b = 1.132$	$b = 1.178$
Confidence interval parameter 1 (PM)	$(0.209 \le a \le 0.219)$	$(0.099 \le a \le 0.103)$	$(0.0159 \le a \le 0.0166)$
Confidence interval parameter 2 (PM)	$(2.109 \le b \le 2.122)$	$(1.123 \le b \le 1.135)$	$(1.177 \le b \le 1.179)$

interpret the FSCFs provided by the pore in the plain specimen, while the generalized extreme value distribution function was found adequate to describe the FSCFs provided by the pore in the VR1 specimen. The FSCFs obtained at the FL with the LM are shown in Fig. 19 together with the fitted curves. The parameters of the fitted curves were obtained with a confidence interval of 80%, and the dashed blue lines shown in Fig. 19 correspond to the envelope of the curves obtained with the parameters at the upper and lower bounds of the chosen confidence interval. The obtained parameters a and b for the distribution function of Gumbel and μ_{gev}, σ_{gev} and ζ for the generalized extreme value distribution function are reported in Table 8 according to the LM and PM. The values corresponding to 99% of probability were then calculated given that using the fatigue stress concentration factors at 99% of probability has been proved to be an efficient solution for flawed materials in Refs. [86,87]. This will be better clarified in the following section.

$$K_{\mathrm{f,VR1,pore}} = \frac{1}{2LK_{\mathrm{f,N}}} \int_0^{2L} \sigma_x \mathrm{d}y \tag{20}$$

$$K'_{\mathrm{f,VR1,pore}} = \frac{\sigma_x\left(\frac{L'}{2}\right)}{K'_{\mathrm{f,N}}} \tag{21}$$

3.3. Fatigue strength predictions

Finally, the results of FSCFs at 99% provided by the surface roughness and the pores were combined for fatigue strength predictions. In the plain as-built specimens the results of the FSCFs were multiplied to calculate the total FSCFs $K_{\mathrm{f,pl,tot}}$ and $K'_{\mathrm{f,pl,tot}}$, according to LM and PM respectively, as described in Eqs. (22) and (23). Given that, as shown in Eq. (23), the form of the equation to calculate the total FSCF according to PM is the same as that to calculate the LM and the variables are only distinguished by the apex ′, for the sake of brevity the expressions to obtain the total FSCFs according to PM are omitted for the other specimens. The same reasoning was applied for the as-built VR1 specimens, and the expression of the total FSCF according to LM is presented in Eq. (24). In the just mentioned expressions $K_{\mathrm{f,pl,pore}}(99\%)$ and $K_{\mathrm{f,VR1,pore}}(99\%)$ were the FSCFs at 99% of probability, obtained with LM and provided by the pores in the plain and VR1 specimens, respectively, while $K_{\mathrm{f,pl,rough}}(99\%)$ and $K_{\mathrm{f,VR1,rough}}(99\%)$ represent the FSCFs at 99% of probability, obtained with LM and provided by the surface roughness in as-built plain and VR1 specimens, respectively. According to Eqs. from (22) to (24), the total FSCFs were computed with the product between the stress concentration factors provided by the pores and the surface roughness. This latter because, according to Figs. 7(d) and (e), the fatigue crack initiation was prone to start from the external surface and the combination between the surface roughness and the pores near the external surface triggered the fatigue failure. As remarked in 3.2, the obtained value of $K_{\mathrm{f,VR1,rough}}$ for the VR1 as-built specimen included the effects of the notch and of the surface roughness, thus three detrimental factors (the notch, the surface roughness and the pores) led to the fatigue failure of the VR1 as-built specimens.

$$K_{\mathrm{f,pl,tot}} = K_{\mathrm{f,pl,pore}}(99\%)\ K_{\mathrm{f,pl,rough}}(99\%) \tag{22}$$

$$K'_{\mathrm{f,pl,tot}} = K'_{\mathrm{f,pl,pore}}(99\%)\ K'_{\mathrm{f,pl,rough}}(99\%) \tag{23}$$

$$K_{\mathrm{f,VR1,tot}} = K_{\mathrm{f,VR1,pore}}(99\%)\ K_{\mathrm{f,VR1,rough}}(99\%) \tag{24}$$

As concerns the plain machined specimen, the total FSCF was still calculated with the product between the FSCFs provided by the surface roughness and internal pores. The obtained expression is presented in Eq. (25) concerning LM. In the just presented expression $K_{\mathrm{f,plm,rough}}(99\%)$ represents the FSCF at 99% of probability, obtained with LM and provided by the surface roughness in machined plain specimens. The FSCFs provided by the pores in the plain machined specimens were the same as that employed for the plain as-built specimen.

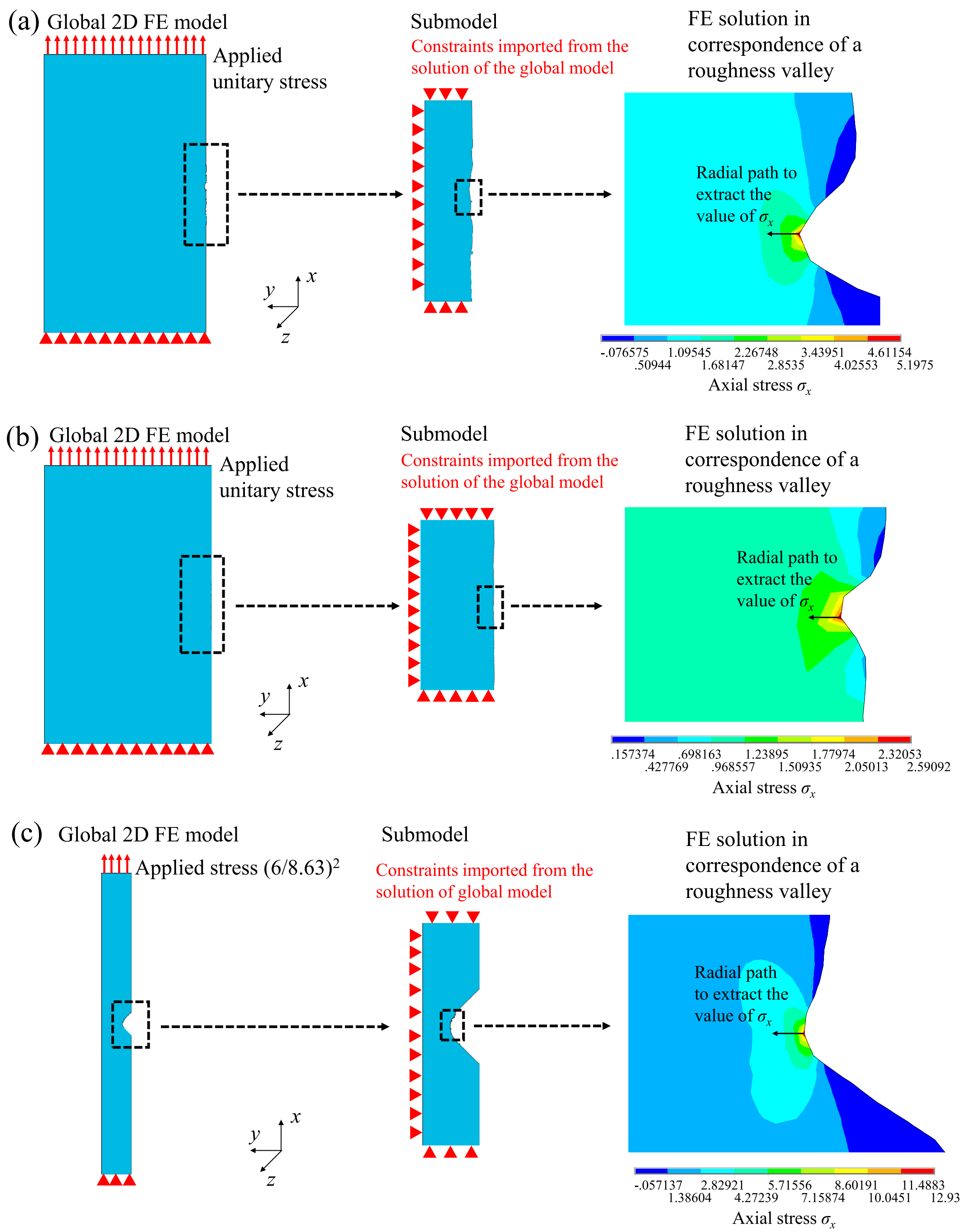

Fig. 16. FE models of the scanned profiles with the results of the axial stress σ_x: (a) plain as-built specimen, (b) plain machined specimen and (c) VR1 as-built specimen.

The value of $K_{\mathrm{f,plm,rough}}(99\%)$ obtained for the plain machined specimen was lower than the corresponding value obtained for the plain as-built specimen as shown in the FE results presented in Figs. 16(a) ad (b). This can be clearly motivated by the fact that the plain machined specimens underwent a machining turning operation to reduce the surface roughness. As described in 3.2 and in Eqs. (20) and (21), the FSCFs for the LM and PM provided by the pore in the VR1machined specimen were computed by relating them to the FSCFs provided by the notch. The intrinsic fatigue curve of the VR1 machined specimen, shown in Fig. 14, corresponds, according to TCD, to the fatigue curves of the intrinsic plain specimen obtained with LM and PM divided by the corresponding FSCFs provided by the notch and calculated with LM and PM, while the experimental fatigue curve of the machined VR1 specimen should correspond to that of the intrinsic machined VR1 specimen divided by the FSCsF provided by the pore calculated with LM and PM. The total FSCFs in the VR1 machined specimen were then equal to Eq. (26) according to LM.

$$K_{\mathrm{f,plm,tot}} = K_{\mathrm{f,pl,pore}}(99\%)\ K_{\mathrm{f,plm,rough}}(99\%) \tag{25}$$

$$K_{\mathrm{f,VR1m,tot}} = K_{\mathrm{f,VR1,pore}}(99\%) \tag{26}$$

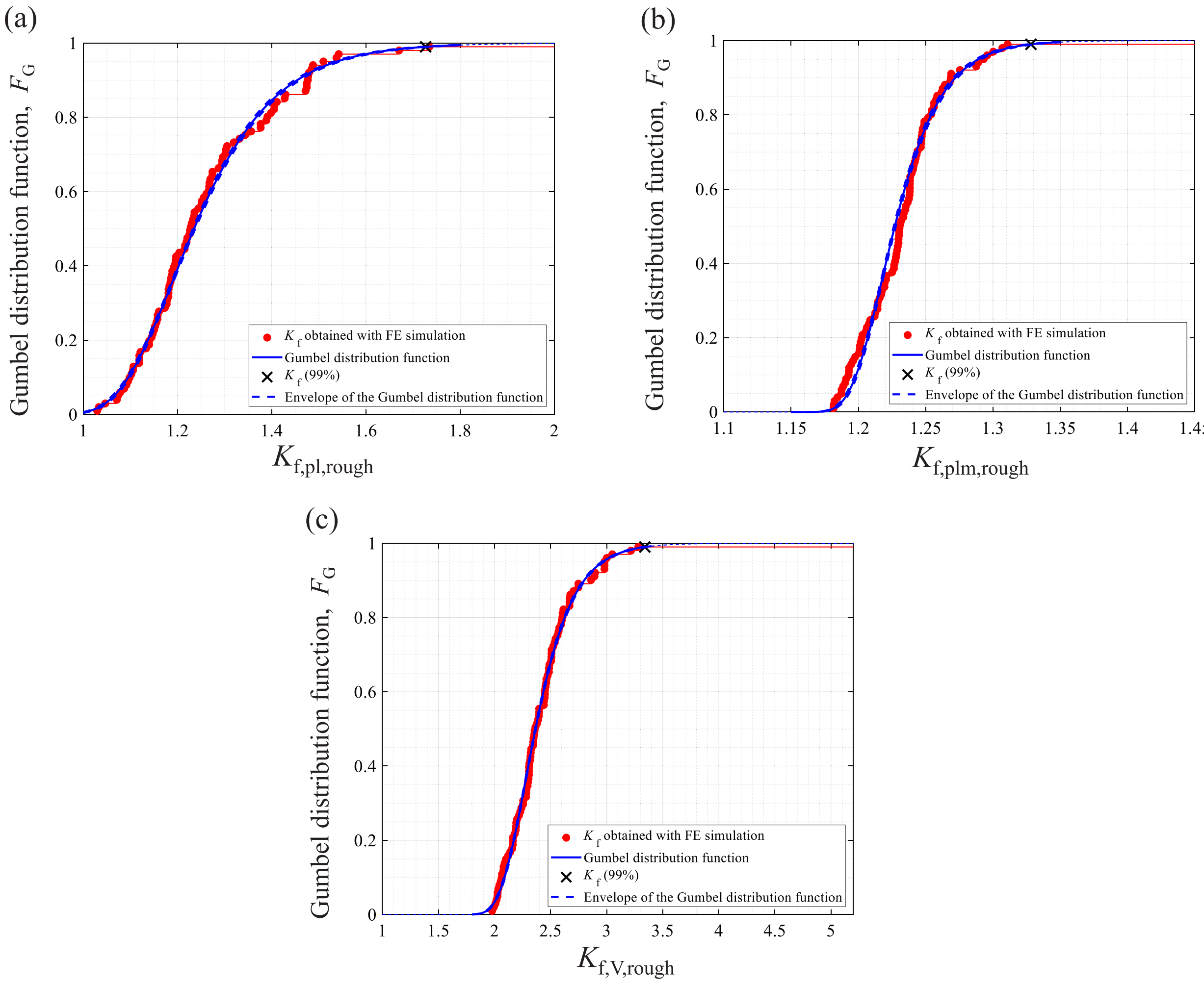

Fig. 17. Statistical analysis of the FSCFs provided by the surface roughness for: (a) plain as-built specimens, (b) plain machined specimens and (c) VR1 as-built specimens.

Table 8
Numerical values obtained for the parameters of the distribution function of Gumbel and generalized extreme value distribution function concerning the FSCFs, calculated with LM and PM, at the FL provided by the pores in the as-built and machined VR1 specimens and the as-built and machined plain specimens.

Quantity	Machined blunt V-notched	As-built and machined plain
Parameter 1 (LM)	$\mu_{gev} = 0.999$	$a = 0.060$
Parameter 2 (LM)	$\sigma_{gev} = 0.0041$	$b = 1.265$
Parameter 3 (LM)	$\zeta = 0.839$	/
Confidence interval parameter 1 (LM)	$(0.998 \le \mu_{gev} \le 1.000)$	$(0.059 \le a \le 0.061)$
Confidence interval parameter 2 (LM)	$(0.0034 \le \sigma_{gev} \le 0.0049)$	$(1.264 \le b \le 1.267)$
Confidence interval parameter 3 (LM)	$(0.698 \le \zeta \le 0.980)$	/
Parameter 1 (PM)	$\mu_{gev} = 0.999$	$a = 0.077$
Parameter 2 (PM)	$\sigma_{gev} = 0.0035$	$b = 1.155$
Parameter 3 (PM)	$\zeta = 0.683$	/
Confidence interval parameter 1 (PM)	$(0.998 \le \mu_{gev} \le 1.000)$	$(0.076 \le a \le 0.078)$
Confidence interval parameter 2 (PM)	$(0.0030 \le \sigma_{gev} \le 0.0041)$	$(1.154 \le b \le 1.156)$
Confidence interval parameter 3 (PM)	$(0.555 \le \zeta \le 0.810)$	/

The predicted number of cycles to failure were computed with an iterative procedure, which considered that the initial input experimental data is the fatigue strength of the considered specimen. Initial guess values of the numbers of cycles to failure were supposed for LM and PM, and they were employed to calculate the values of the critical distances and the corresponding FSCFs, which were multiplied by the input fatigue strength to estimate the intrinsic fatigue strength. These latter values were used in the SN curves of the intrinsic fatigue strength according to LM and PM to calculate the number of cycles to failure. If the difference between the updated numbers of cycles to failure and the previous value was below an imposed tolerance, the procedure stopped and the predicted numbers of cycles to failure according to LM and PM were obtained. Otherwise, the critical distances and the corresponding values of the FSCFs were updated at the newly obtained number of cycles to failure, and the procedure was repeated until the difference between the number of cycles to failure obtained at the steps i and $i+1$ was lower than an imposed tolerance. The predicted fatigue strength values were calculated for the plain as-built specimens as described in Eqs. (27) and (28) for LM and PM, respectively. As for the total FSCFs, the form of the equations to calculate the fatigue strength according to LM and PM were the same and the variables were distinguished by the apex $'$. For this reason and for the sake of brevity, the expressions

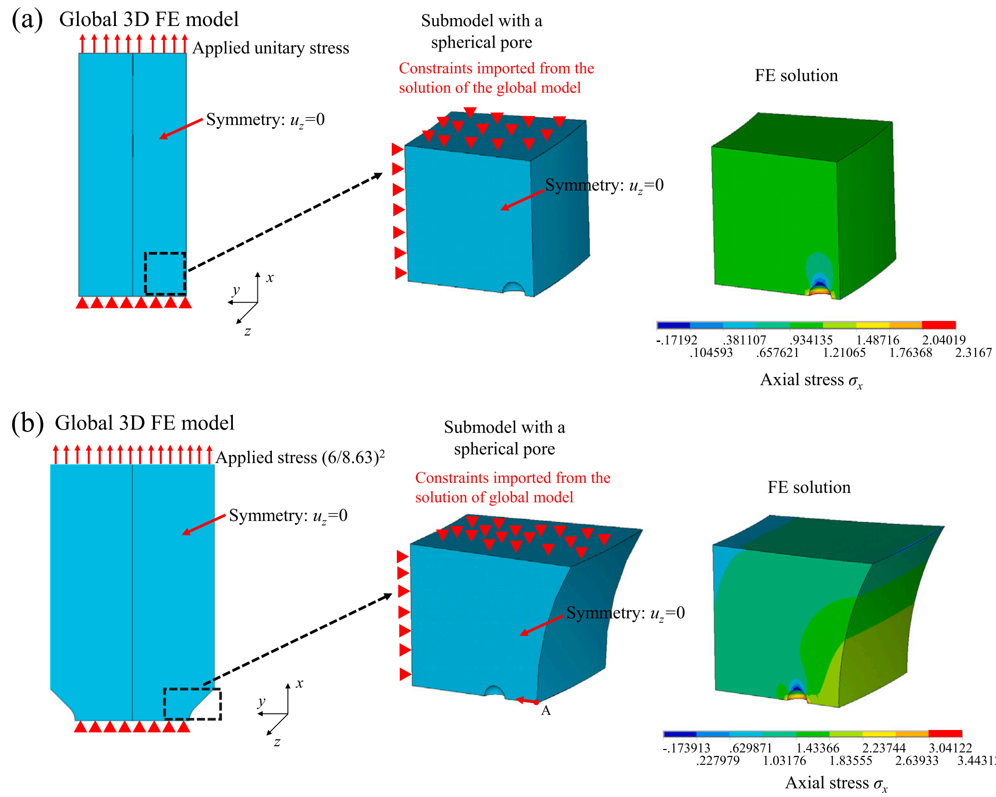

Fig. 18. FE models of the pores with the axial stress results σ_x: (a) plain specimen, (b) VR1 specimen.

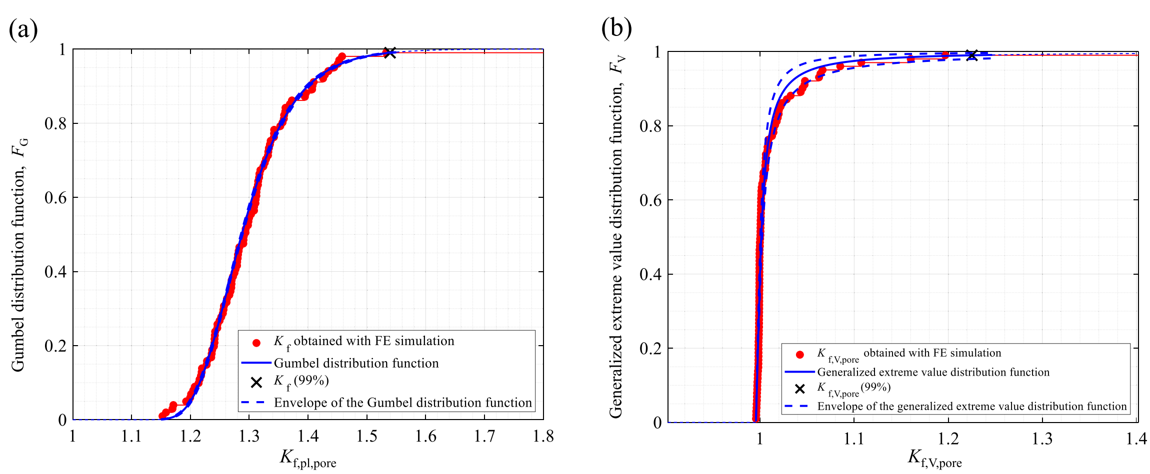

Fig. 19. Statistical analysis of the FSCFs provided by the pores for: (a) plain specimen and (b) VR1 specimen.

to calculate the fatigue strength according to PM are omitted for all the other specimens. The expressions to calculate the fatigue strength of the plain machined specimen, the as-built VR1 specimen and the machined VR1 specimen are presented in Eqs. (29), (30) and (31), respectively. In Eq. (31) $\sigma^*_{a,VR1}$ represents the fatigue strength of the intrinsic VR1 machined specimen. The logic flow behind the procedure proposed in this research to calculate the fatigue strength and the number of cycles to failure of unnotched and notched specimens of Inconel 718, manufactured with LPBF and in machined and as-built surface conditions is resumed in Fig. 20.

$$\sigma_{a,pred,pl} = \sigma^*_a / K_{f,pl,tot} \tag{27}$$

$$\sigma'_{a,pred,pl} = \sigma^{*\prime}_a / K'_{f,pl,tot} \tag{28}$$

$$\sigma_{a,pred,plm} = \sigma^*_a / K_{f,plm,tot} \tag{29}$$

$$\sigma_{a,pred,VR1} = \sigma^*_a / K_{f,VR1,tot} \tag{30}$$

$$\sigma_{a,pred,VR1m} = \sigma^*_{a,VR1} / K_{f,VR1m,tot} \tag{31}$$

4. Discussion

The obtained values of the critical distances L and L' according to LM and PM, respectively, and presented in Fig. 15(a) show that $L' \approx 2L$. This result therefore confirms what obtained by Santus et al.

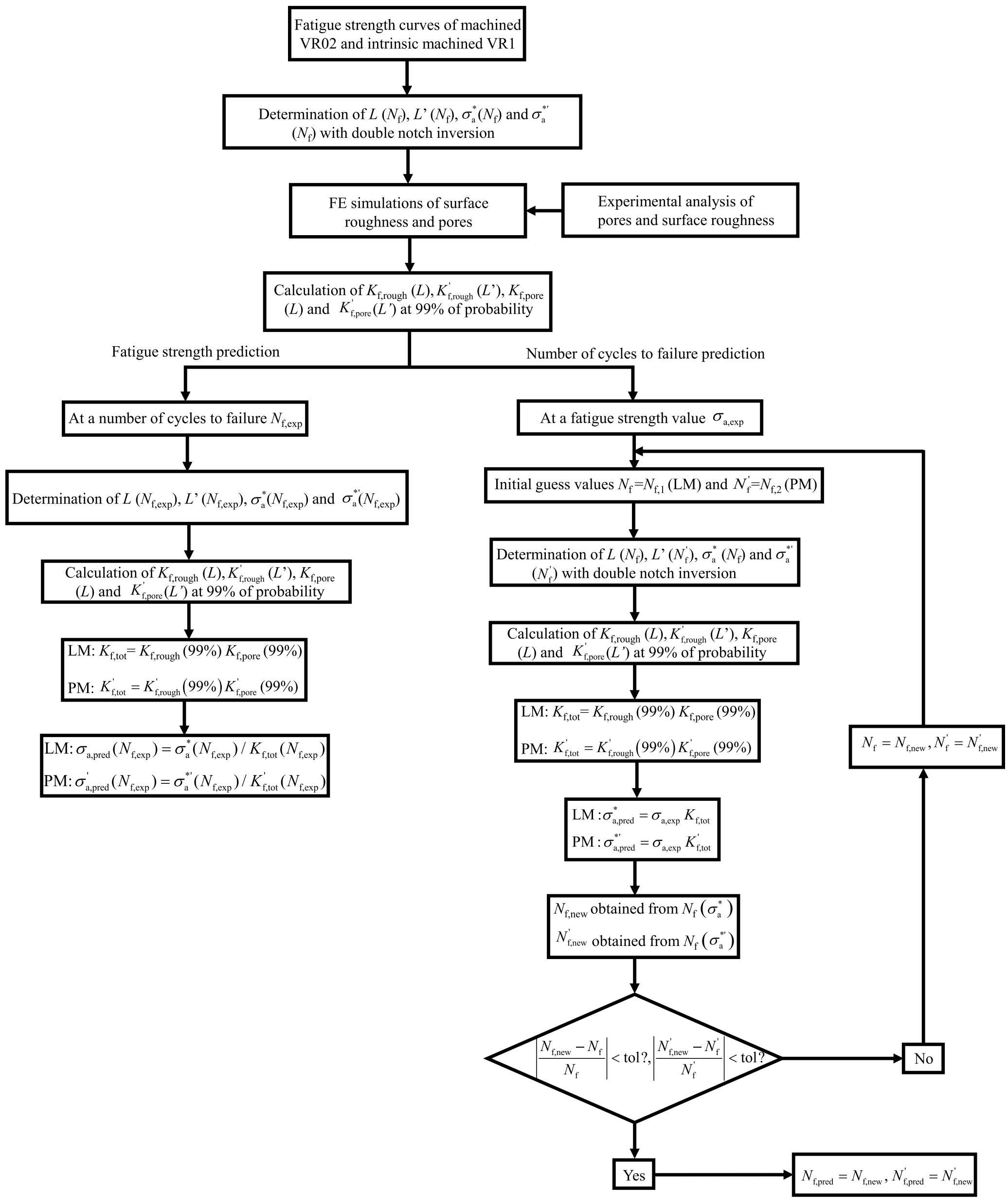

Fig. 20. Logic flow of the proposed procedure.

Table 9
Comparisons between experimental and predicted values of the FL for the different types of specimens.

Specimen type	Exp. FL MPa	Pred. FL (LM) MPa	Err. (LM) (%)	Pred. FL (PM) MPa	Err. (PM) (%)
Blunt V-notched machined	146	154	5.50	171	17.2
Cylindrical as-built	132	146	10.6	161	22
Cylindrical machined	205	190	−7.30	207	0.98
Blunt V-notched as-built	100	94.6	−4.40	113	14.1

in Ref. [39]. In addition, when TCD is applied, the intrinsic fatigue strength, for both LM and PM, coincides with the fatigue strength of the plain machined specimen. In this case, given the detrimental presence of pores near the crack initiation sites in plain machined specimens, these latter were not considered as the intrinsic specimens. The values of the intrinsic fatigue strengths were therefore calculated by applying the double notch inversion procedure, and there could be indeterminacy given that different values can be obtained with LM and PM. Despite this, in the current research the values of the intrinsic fatigue strength σ_a^* and $\sigma_a^{*'}$ obtained with LM and PM, respectively, were very similar as confirmed in Fig. 15(b). This latter results confirms the robustness of the double notch inversion procedure to calculate the values of the critical distances and of the intrinsic fatigue strength when the presence of internal defects is detrimental for the fatigue failure of the plain machined specimens. The obtained results in terms of predicted number of cycles to failure and fatigue strength, and obtained with LM and PM, are shown in Fig. 21 where the bisector corresponds to a hypothetical perfect correspondence between the predicted and experimental quantities, while the dashed lines represent the multiplicative factors 2 and 3 as concerns the number of cycles to failure and the errors of ±10% and ±20% regarding the fatigue strength. In addition, the predicted fatigue strength at the FL are resumed in Table 9 for all the specimens. In the obtained results it is highlighted that the PM overestimates the fatigue strength and the number of cycles to failure

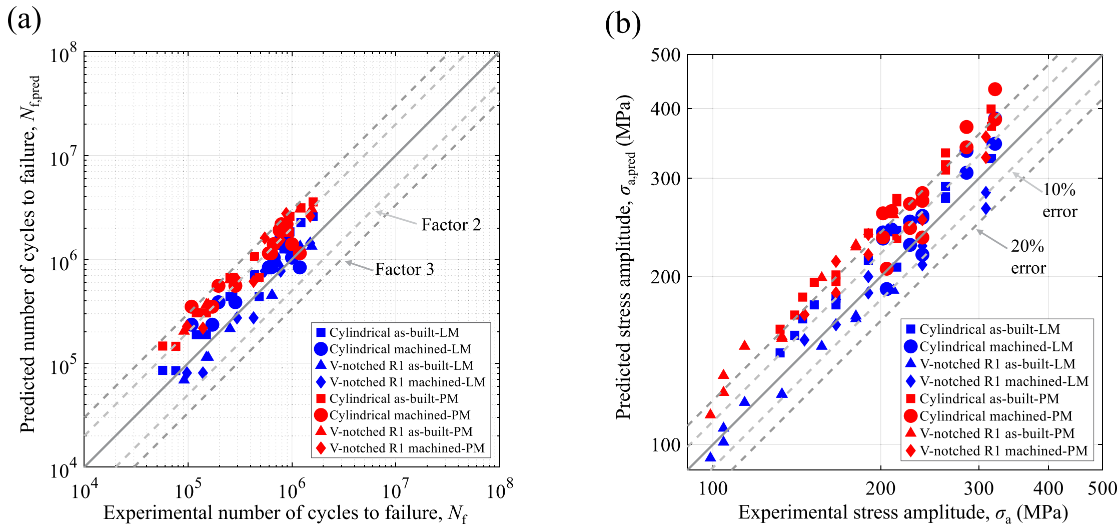

Fig. 21. (a) Comparisons between the predicted and experimental numbers of cycles to failure and (b) comparison between the predicted and experimental fatigue strength values.

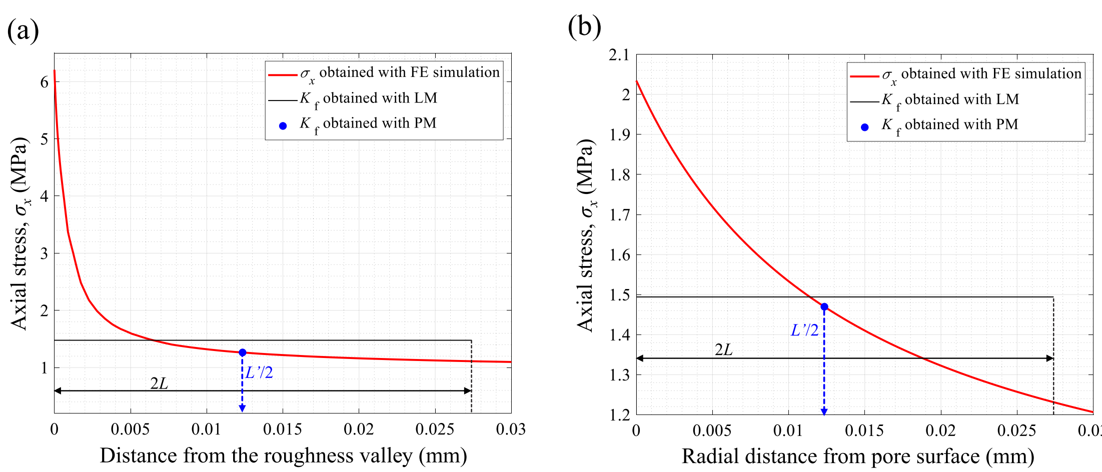

Fig. 22. Examples of obtained K_f values with LM and PM for (a) the surface roughness and (b) the pores.

with respect to the experimental data. Given that, as discussed above, the calculated intrinsic fatigue strength values were almost similar between LM and PM, the reasons of these forecast discrepancies are to attributed to the different obtained values of the FSCFs according to LM and PM. In particular, given that the PM overestimate the predicted fatigue strength and number of cycles to failure, the FSCFs computed with PM were clearly lower than the corresponding FSCFs calculated with LM. This can be motivated by observing Fig. 22 where two plots of the axial stress σ_x obtained from FE simulation of the surface roughness (Fig. 22(a)) and the pores (Fig. 22(b)) are presented. In this figure, the results of the FSCFs calculated with LM and PM are reported and it is evident that PM underestimate the FSCFs, especially those provided by the surface roughness. After FE simulation of the surface profiles obtained with the optical profilometer, it was obtained that the roughness valleys act as micro-notches with a highly concentrated stress and a very steep gradient. A shown in Fig. 22(a), the point where the stress was extracted according to PM was out of the initial zone with the steep gradient, thus the PM was not able to properly capture this high slope of the stress. On the other side, the LM proposes to evaluate the FSCF as the average integral on the micro-notch bisector of the roughness valley and starting from the roughness valley until a distance of $2L$ from the initial point. For these reasons, the initial zone with the high slope has been necessarily considered during the computation of the FSCFs with LM. The FE simulations of the pores in both the plain and the VR1 specimens, highlighted a lower gradient of the axial stress, thus the differences between the FSCFs calculated with LM and PM were lower than the corresponding values obtained during the analysis of the surface roughness. In any case, also in the pores analysis, the FSCFs computed with LM were higher than those obtained with PM.

5. Conclusions

In this research the fatigue strength of plain and V-notched (blunt and sharp) specimens made of Inconel 718 and manufactured with LPBF was investigated. The specimens underwent an aging treatment to increase the hardness after the 3D printing process, and two surface conditions were investigated: the as-built, for the blunt V-notched and the plain specimens, and the machined for the sharp V-notched, the blunt V-notched and the plain specimens. The surface machined condition was obtained after a turning machining operation at the end of the aging treatment. A probabilistic method, based on TCD (LM and PM), was proposed to calculate the FSCFs provided by the surface roughness and the internal pores. The main findings of the research are summarized below.

- Given the detrimental effect of internal pores on the fatigue strength of plain machined specimens, the critical distances were obtained with the double notch inversion, thus involving the machined sharp and blunt V-notched specimens. The employed mathematical procedure was that proposed in Ref. [39].

- Cross sectional analyses were performed to investigate the internal pores of the specimens. It was obtained that the distribution function of Gumbel and the exponential distribution function can accurately model the distributions of the pore diameter and of the distance from the external surface, respectively, in the plain specimens. On the other side, it was found that the generalized extreme value distribution function can accurately model the distributions of the pore diameter and of the distance from the external surface in the blun V-notched specimens.
- Two populations of pore diameter and distance from the external surface were generated for the plain specimen and the V-notched specimen starting from the identified probability distributions. After that, FE models were implemented to simulate the generated population of pores, and the FSCFs were calculated with TCD.
- The optical profilometer was employed to investigate the surface morphology, and the obtained surface profiles were used to perform FE simulations. The FSCFs provided by the surface roughness were then calculated by using TCD.
- The distributions of the obtained stress concentration factors provided by the pore and the surface roughness were fitted with the distribution function of Gumbel or with the generalized extreme value distribution function, and the values at 99% of probability were extracted.
- Given that the inspections of the fractured surfaces revealed a combination of the pores and the surface roughness in triggering the fatigue failure, the total FSCF was obtained as the product between the FSCF of the pores and the FSCF of the surface roughness for the machined and as-built plain specimens and for the as-built blunt V-notched specimen. The total FSCF was, instead, equal to that of the pore in the machined blunt V-notched specimen given that the effect of the surface roughness was negligible and, in any case, already considered in the notch effect.
- The predictions of the fatigue strength and of the number of cycles to failure performed with LM provided good agreement with experimental data and a better accuracy than the corresponding predictions obtained with PM. This because the PM cannot properly capture the rapid gradient of the stress provided by the micro-notches of the surface roughness.
- According to Fig. 15(b), the intrinsic fatigue strength obtained with the inverse procedure proposed by Santus et al. in Ref. [39] is appreciably higher, almost twice, than that of the machined plain specimen. This means that the reduction of the surface roughness and the almost total elimination of the internal pores can have a significant impact on the fatigue strength of the AM materials.
- The approach proposed in this research to calculate the critical distances and the FSCFs provided by the surface roughness and the internal pores can then be applied to assess the fatigue strength of AM mechanical components.

CRediT authorship contribution statement

Lorenzo Romanelli: Writing – review & editing, Writing – original draft, Validation, Software, Methodology, Investigation, Data curation, Conceptualization. **Ciro Santus:** Writing – review & editing, Writing – original draft, Validation, Supervision, Methodology, Investigation, Conceptualization. **Giuseppe Macoretta:** Writing – review & editing, Validation, Supervision, Methodology, Investigation, Conceptualization. **Michele Barsanti:** Writing – review & editing, Writing – original draft, Software, Methodology, Investigation, Conceptualization. **Bernardo Disma Monelli:** Writing – review & editing, Supervision, Methodology, Investigation, Data curation. **Ivan Senegaglia:** Writing – review & editing, Methodology, Investigation. **Adrian Hugh Alexander Lutey:** Writing – review & editing, Validation, Software, Methodology, Investigation, Data curation. **Hossein Rajaei:** Writing – review & editing, Writing – original draft, Software, Methodology, Investigation, Data curation. **Cinzia Menapace:** Writing – review & editing, Writing – original draft, Methodology, Investigation, Data curation, Conceptualization. **Matteo Benedetti:** Writing – review & editing, Writing – original draft, Supervision, Software, Methodology, Investigation, Data curation, Conceptualization.

Declaration of competing interest

The authors declare that they have no known competing financial interests or personal relationships that could have appeared to influence the work reported in this paper.

Acknowledgements

This work was financially supported by the Italian Ministry of University and Research (MUR) in the frame of the programme PNRR_ Piano Nazionale di Ripresa e Resilienza – MISSIONE 4 COMPONENTE 2, "Dalla ricerca all'impresa" INVESTIMENTO 1.1, "Fondo per il Programma Nazionale di Ricerca e Progetti di Rilevante Interesse Nazionale (PRIN)", project title "RePowder: recycled powder for sustainable metal additive manufacturing", grant number P2022MEFCJ. Website of the project: https://www.repowder.it/.

Data availability

Data will be made available on request.

References

[1] Wang X, Gong X, Chou K. Review on powder-bed laser additive manufacturing of Inconel 718 parts. In: Volume 1: processing. American Society of Mechanical Engineers; 2015, http://dx.doi.org/10.1115/msec2015-9322.
[2] Debarbadillo JJ, Mannan SK. Alloy 718 for oilfield applications. JOM 2012;64:265–70, URL https://api.semanticscholar.org/CorpusID:54670040.
[3] Pratheesh Kumar S, Elangovan S, Mohanraj R, Ramakrishna JR. A review on properties of Inconel 625 and Inconel 718 fabricated using direct energy deposition. Mater Today: Proc 2021;46:7892–906. http://dx.doi.org/10.1016/j.matpr.2021.02.566.
[4] Cersullo N, Mardaras J, Emile P, Nickel K, Holzinger V, Hühne C. Effect of internal defects on the fatigue behavior of additive manufactured metal components: a comparison between Ti6Al4V and Inconel 718. Materials 2022;15(19):6882. http://dx.doi.org/10.3390/ma15196882.
[5] Hosseini E, Popovich VA. A review of mechanical properties of additively manufactured Inconel 718. Addit Manuf 2019;30:100877. http://dx.doi.org/10.1016/j.addma.2019.100877.
[6] Georges H, Mittelstedt C, Becker W. RVE-based grading of truss lattice cores in sandwich panels. Arch Appl Mech 2023;93(8):3189–203. http://dx.doi.org/10.1007/s00419-023-02432-1.
[7] Großmann A, Klyk M, Kohn L, Meyer G, Greiner M, Yang Y, Mittelstedt C. Bioinspired airwings: Design and additive manufacturing of a geometrically graded microscale maple seed. Mater Today Commun 2024;38:108014. http://dx.doi.org/10.1016/j.mtcomm.2023.108014.
[8] Philpott W, Jepson MAE, Thomson RC. Comparison of the effects of a conventional heat treatment between cast and selective laser melted IN939 alloy. 2016, p. 735–46.
[9] Khanna N, Zadafiya K, Patel T, Kaynak Y, Rahman Rashid RA, Vafadar A. Review on machining of additively manufactured nickel and titanium alloys. J Mater Res Technol 2021;15:3192–221. http://dx.doi.org/10.1016/j.jmrt.2021.09.088.
[10] Benedetti M, Santus C. Notch fatigue and crack growth resistance of Ti-6Al-4V ELI additively manufactured via selective laser melting: A critical distance approach to defect sensitivity. Int J Fatigue 2019;121:281–92. http://dx.doi.org/10.1016/j.ijfatigue.2018.12.020.
[11] Liu SY, Li HQ, Qin CX, Zong R, Fang XY. The effect of energy density on texture and mechanical anisotropy in selective laser melted Inconel 718. Mater Des 2020;191:108642. http://dx.doi.org/10.1016/j.matdes.2020.108642.
[12] Balbaa M, Mekhiel S, Elbestawi M, McIsaac J. On selective laser melting of Inconel 718: Densification, surface roughness, and residual stresses. Mater Des 2020;193:108818. http://dx.doi.org/10.1016/j.matdes.2020.108818.
[13] Tucho WM, Cuvillier P, Sjolyst-Kverneland A, Hansen V. Microstructure and hardness studies of Inconel 718 manufactured by selective laser melting before and after solution heat treatment. Mater Sci Eng A 2017;689:220–32. http://dx.doi.org/10.1016/j.msea.2017.02.062.

[14] Watring DS, Carter KC, Crouse D, Raeymaekers B, Spear AD. Mechanisms driving high-cycle fatigue life of as-built Inconel 718 processed by laser powder bed fusion. Mater Sci Eng A 2019;761:137993. http://dx.doi.org/10.1016/j.msea.2019.06.003.

[15] Sola A, Nouri A. Microstructural porosity in additive manufacturing: The formation and detection of pores in metal parts fabricated by powder bed fusion. J Adv Manuf Process 2019;1(3). http://dx.doi.org/10.1002/amp2.10021.

[16] Witkin DB, Patel D, Albright TV, Bean GE, McLouth T. Influence of surface conditions and specimen orientation on high cycle fatigue properties of Inconel 718 prepared by laser powder bed fusion. Int J Fatigue 2020;132:105392. http://dx.doi.org/10.1016/j.ijfatigue.2019.105392.

[17] Guo C, Li S, Shi S, Li X, Hu X, Zhu Q, et al. Effect of processing parameters on surface roughness, porosity and cracking of as-built IN738LC parts fabricated by laser powder bed fusion. J Mater Process Technol 2020;285:116788. http://dx.doi.org/10.1016/j.jmatprotec.2020.116788.

[18] Stopka KS, Desrosiers A, Nicodemus T, Krutz N, Andreaco A, Sangid MD. Intentionally seeding pores in additively manufactured alloy 718: Process parameters, microstructure, defects, and fatigue. Addit Manuf 2023;66:103450. http://dx.doi.org/10.1016/j.addma.2023.103450.

[19] Uriati F, Nicoletto G, Lutey AHA. As-built surface quality and fatigue resistance of Inconel 718 obtained by additive manufacturing. Mater Des Process Commun 2021;3(4). http://dx.doi.org/10.1002/mdp2.228.

[20] Dinh TD, Han S, Yaghoubi V, Xiang H, Erdelyi H, Craeghs T, et al. Modeling detrimental effects of high surface roughness on the fatigue behavior of additively manufactured Ti-6Al-4V alloys. Int J Fatigue 2021;144:106034. http://dx.doi.org/10.1016/j.ijfatigue.2020.106034.

[21] Lee S, Rasoolian B, Silva DF, Pegues JW, Shamsaei N. Surface roughness parameter and modeling for fatigue behavior of additive manufactured parts: A non-destructive data-driven approach. Addit Manuf 2021;46:102094. http://dx.doi.org/10.1016/j.addma.2021.102094.

[22] Afazov S, Serjouei A, Hickman GJ, Mahal R, Goy D, Mitchell I. Defect-based fatigue model for additive manufacturing. Prog Addit Manuf 2022;8(5):1059–66. http://dx.doi.org/10.1007/s40964-022-00376-6.

[23] Macek W, Marciniak Z, Lesiuk G, Podulka P, Jiang C-P. The Smith-Watson-Topper parameter and fracture surface topography relationship for additively manufactured 18Ni300 steel subjected to uniaxial variable-amplitude loading. Theor Appl Fract Mech 2024;133:104607. http://dx.doi.org/10.1016/j.tafmec.2024.104607.

[24] Taylor D. The theory of critical distances. Eng Fract Mech 2008;75(7):1696–705. http://dx.doi.org/10.1016/j.engfracmech.2007.04.007.

[25] Taylor D. The theory of critical distances. Elsevier Science; 2007, http://dx.doi.org/10.1016/B978-0-08-044478-9.X5000-5.

[26] Susmel L, Taylor D. A simplified approach to apply the theory of critical distances to notched components under torsional fatigue loading. Int J Fatigue 2006;28(4):417–30. http://dx.doi.org/10.1016/j.ijfatigue.2005.07.035.

[27] Susmel L, Taylor D. The Theory of Critical Distances to estimate finite lifetime of notched components subjected to constant and variable amplitude torsional loading. Eng Fract Mech 2013;98:64–79. http://dx.doi.org/10.1016/j.engfracmech.2012.12.007.

[28] Benedetti M, Santus C. Mean stress and plasticity effect prediction on notch fatigue and crack growth threshold. Comb Theory Crit Distances Multiaxial Fatigue Criteria Fatigue Fract Eng Mater Struct 2018;42(6):1228–46. http://dx.doi.org/10.1111/ffe.12910.

[29] Santus C, Berto F, Pedranz M, Benedetti M. Mode III critical distance determination with optimized V-notched specimen under torsional fatigue and size effects on the inverse search probability distribution. Int J Fatigue 2021;151:106351. http://dx.doi.org/10.1016/j.ijfatigue.2021.106351.

[30] Łagoda T, Vantadori S, Głowacka K, Kurek M, Kluger K. Using the smith-watson-topper parameter and its modifications to calculate the fatigue life of metals: the state-of-the-art. Materials 2022;15(10):3481. http://dx.doi.org/10.3390/ma15103481.

[31] Santus C, Romanelli L, Grossi T, Neri P, Romoli L, Lutey AHA, et al. Torsional-loaded notched specimen fatigue strength prediction based on mode I and mode III critical distances and fracture surface investigations with a 3D optical profilometer. Int J Fatigue 2022;161:106913. http://dx.doi.org/10.1016/j.ijfatigue.2022.106913.

[32] Santus C, Romanelli L, Grossi T, Bertini L, Le Bone L, Chiesi F, et al. Elastic–plastic analysis of high load ratio fatigue tests on a shot-peened quenched and tempered steel, combining the Chaboche model and the Theory of Critical Distances. Int J Fatigue 2023;174:107713. http://dx.doi.org/10.1016/j.ijfatigue.2023.107713.

[33] Shamsaei N, Fatemi A, Socie DF. Multiaxial fatigue evaluation using discriminating strain paths. Int J Fatigue 2011;33(4):597–609. http://dx.doi.org/10.1016/j.ijfatigue.2010.11.002.

[34] Fatemi A, Shamsaei N. Multiaxial fatigue: An overview and some approximation models for life estimation. Int J Fatigue 2011;33(8):948–58. http://dx.doi.org/10.1016/j.ijfatigue.2011.01.003.

[35] Liao D, Zhu S-P, Qian G. Multiaxial fatigue analysis of notched components using combined critical plane and critical distance approach. Int J Mech Sci 2019;160:38–50. http://dx.doi.org/10.1016/j.ijmecsci.2019.06.027.

[36] He J-C, Zhu S-P, Gao J-W, Liu R, Li W, Liu Q, et al. Microstructural size effect on the notch fatigue behavior of a Ni-based superalloy using crystal plasticity modelling approach. Int J Plast 2024;172:103857. http://dx.doi.org/10.1016/j.ijplas.2023.103857.

[37] Wu X. On Tanaka-Mura's fatigue crack nucleation model and validation. Fatigue Fract Eng Mater Struct 2017;41(4):894–9. http://dx.doi.org/10.1111/ffe.12736.

[38] He J-C, Zhu S-P, Luo C, Li W, Liu Q, He Y, et al. Probabilistic notch fatigue assessment under size effect using micromechanics-based critical distance theory. Int J Fatigue 2024;183:108280. http://dx.doi.org/10.1016/j.ijfatigue.2024.108280.

[39] Santus C, Taylor D, Benedetti M. Determination of the fatigue critical distance according to the Line and the Point Methods with rounded V-notched specimen. Int J Fatigue 2018;106:208–18. http://dx.doi.org/10.1016/j.ijfatigue.2017.10.002.

[40] Gillham B, Yankin A, McNamara F, Tomonto C, Taylor D, Lupoi R. Application of the Theory of Critical Distances to predict the effect of induced and process inherent defects for SLM Ti-6Al-4V in high cycle fatigue. CIRP Ann 2021;70(1):171–4. http://dx.doi.org/10.1016/j.cirp.2021.03.004.

[41] Dinh TD, Vanwalleghem J, Xiang H, Erdelyi H, Craeghs T, Paepegem WV. A unified approach to model the effect of porosity and high surface roughness on the fatigue properties of additively manufactured Ti6-Al4-V alloys. Addit Manuf 2020;33:101139. http://dx.doi.org/10.1016/j.addma.2020.101139.

[42] Murakami Y. Metal fatigue. Elsevier; 2019, http://dx.doi.org/10.1016/c2016-0-05272-5.

[43] Santus C, Romanelli L, Bertini L, Burchianti A, Inoue T. Resonant fatigue tests on polished drill pipe specimens. Machines 2024;12(5):314. http://dx.doi.org/10.3390/machines12050314.

[44] Chapetti MD. Fracture mechanics for fatigue design of metallic components and small defect assessment. Int J Fatigue 2022;154:106550. http://dx.doi.org/10.1016/j.ijfatigue.2021.106550.

[45] Zhang J, Fatemi A. Surface roughness effect on multiaxial fatigue behavior of additive manufactured metals and its modeling. Theor Appl Fract Mech 2019;103:102260. http://dx.doi.org/10.1016/j.tafmec.2019.102260.

[46] Macoretta G, Bertini L, Monelli BD, Berto F. Productivity-oriented SLM process parameters effect on the fatigue strength of Inconel 718. Int J Fatigue 2023;168:107384. http://dx.doi.org/10.1016/j.ijfatigue.2022.107384.

[47] Rigon D, Coppola F, Meneghetti G. Fracture mechanics-based analysis of the fatigue limit of Ti6Al4V alloy specimens manufactured by SLM in as-built surface conditions by means of areal measurements. Eng Fract Mech 2024;295:109720. http://dx.doi.org/10.1016/j.engfracmech.2023.109720.

[48] Newman JC, Raju IS. Stress-intensity factor equations for cracks in three-dimensional finite bodies. PO Box C700, West Conshohocken, PA 19428-2959: ASTM International100 Barr Harbor Drive; 1983, p. 238–65. http://dx.doi.org/10.1520/stp37074s.

[49] Yamashita Y, Murakami T, Mihara R, Okada M, Murakami Y. Defect analysis and fatigue design basis for Ni-based superalloy 718 manufactured by additive manufacturing. Procedia Struct Integr 2017;7:11–8. http://dx.doi.org/10.1016/j.prostr.2017.11.054.

[50] Yamashita Y, Murakami T, Mihara R, Okada M, Murakami Y. Defect analysis and fatigue design basis for Ni-based superalloy 718 manufactured by selective laser melting. Int J Fatigue 2018;117:485–95. http://dx.doi.org/10.1016/j.ijfatigue.2018.08.002.

[51] Zanini F, Sbettega E, Carmignato S. X-ray computed tomography for metal additive manufacturing: challenges and solutions for accuracy enhancement. Procedia CIRP 2018;75:114–8. http://dx.doi.org/10.1016/j.procir.2018.04.050.

[52] Wang J, Cui Y, Liu C, Li Z, Wu Q, Fang D. Understanding internal defects in Mo fabricated by wire arc additive manufacturing through 3D computed tomography. J Alloys Compd 2020;840:155753. http://dx.doi.org/10.1016/j.jallcom.2020.155753.

[53] Shahabi M, Reddy T, Rollett AD, Narra SP. A statistical approach to determine data requirements for part porosity characterization in laser powder bed fusion additive manufacturing. Mater Charact 2022;190:112027. http://dx.doi.org/10.1016/j.matchar.2022.112027.

[54] Pedranz M, Fontanari V, Raghavendra S, Santus C, Zanini F, Carmignato S, et al. A new energy based highly stressed volume concept to investigate the notch-pores interaction in thick-walled ductile cast iron subjected to uniaxial fatigue. Int J Fatigue 2023;169:107491. http://dx.doi.org/10.1016/j.ijfatigue.2022.107491.

[55] Benedetti M, Pedranz M, Fontanari V, Menapace C, Bandini M. Enhancing plain fatigue strength in aluminum alloys through shot peening: Experimental investigations and a strain energy density interpretation. Int J Fatigue 2024;184:108299. http://dx.doi.org/10.1016/j.ijfatigue.2024.108299.

[56] Ai Y, Zhu S-P, Liao D, Correia JAFO, De Jesus AMP, Keshtegar B. Probabilistic modelling of notch fatigue and size effect of components using highly stressed volume approach. Int J Fatigue 2019;127:110–9. http://dx.doi.org/10.1016/j.ijfatigue.2019.06.002.

[57] Niu X, Zhu S-P, He J-C, Liao D, Correia JAFO, Berto F, et al. Defect tolerant fatigue assessment of AM materials: Size effect and probabilistic prospects. Int J Fatigue 2022;160:106884. http://dx.doi.org/10.1016/j.ijfatigue.2022.106884.

[58] Niu X, Zhu S-P, He J-C, Luo C, Wang Q. Probabilistic and defect tolerant fatigue assessment of AM materials under size effect. Eng Fract Mech 2023;277:109000. http://dx.doi.org/10.1016/j.engfracmech.2022.109000.

[59] Macek W, Masoudi Nejad R, Zhu S-P, Trembacz J, Branco R, Costa JDM, et al. Effect of bending-torsion on fracture and fatigue life for 18Ni300 steel specimens produced by SLM. Mech Mater 2023;178:104576. http://dx.doi.org/10.1016/j.mechmat.2023.104576.

[60] Macek W, Tomczyk A, Branco R, Dobrzyński M, Seweryn A. Fractographical quantitative analysis of EN-AW 2024 aluminum alloy after creep pre-strain and LCF loading. Eng Fract Mech 2024;282(2023):109182. http://dx.doi.org/10.1016/j.engfracmech.2023.109182.

[61] Macek W, Rozumek D, Faszynka S, Branco R, Zhu S-P, Masoudi Nejad R. Fractographic-fractal dimension correlation with crack initiation and fatigue life for notched aluminium alloys under bending load. Eng Fail Anal 2023;149:107285. http://dx.doi.org/10.1016/j.engfailanal.2023.107285.

[62] Macek W, Branco R, Podulka P, Masoudi Nejad R, Costa JD, Ferreira JAM, et al. The correlation of fractal dimension to fracture surface slope for fatigue crack initiation analysis under bending-torsion loading in high-strength steels. Measurement 2023;218:113169. http://dx.doi.org/10.1016/j.measurement.2023.113169.

[63] Nicoletto G, Tinelli G, Lutey AHA, Romoli L. Influence of as-built surface topography on the fatigue behavior of SLM Inconel 718 : experiments and modeling. In: II international conference on simulation for additive manufacturing. 2019.

[64] Moda M, Chiocca A, Macoretta G, Monelli BD, Bertini L. Technological implications of the Rosenthal solution for a moving point heat source in steady state on a semi-infinite solid. Mater Des 2022;223:110991. http://dx.doi.org/10.1016/j.matdes.2022.110991.

[65] Macoretta G, Romanelli L, Santus C, Romoli L, Lutey AHA, Uriati F, et al. Modelling of the surface morphology and size effects on fatigue strength of L-PBF Inconel 718 by comparing different testing specimens. Int J Fatigue 2024;181:108120. http://dx.doi.org/10.1016/j.ijfatigue.2023.108120.

[66] Zhang D, Niu W, Cao X, Liu Z. Effect of standard heat treatment on the microstructure and mechanical properties of selective laser melting manufactured Inconel 718 superalloy. Mater Sci Eng A 2015;644:32–40. http://dx.doi.org/10.1016/j.msea.2015.06.021.

[67] Barros R, Silva FJG, Gouveia RM, Saboori A, Marchese G, Biamino S, et al. Laser powder bed fusion of Inconel 718: residual stress analysis before and after heat treatment. Metals 2019;9(12):1290. http://dx.doi.org/10.3390/met9121290.

[68] Marchese G, Atzeni E, Salmi A, Biamino S. Microstructure and residual stress evolution of laser powder bed fused Inconel 718 under heat treatments. J Mater Eng Perform 2020;30(1):565–74. http://dx.doi.org/10.1007/s11665-020-05338-z.

[69] Oradei-Basile A, Radavich JF. A current T-T-T diagram for wrought alloy 718. In: Superalloys 718, 625 and various derivatives (1991). TMS; 1991, p. 325–35. http://dx.doi.org/10.7449/1991/superalloys_1991_325_335.

[70] Aydinöz ME, Brenne F, Schaper M, Schaak C, Tillmann W, Nellesen J, et al. On the microstructural and mechanical properties of post-treated additively manufactured Inconel 718 superalloy under quasi-static and cyclic loading. Mater Sci Eng A 2016;669:246–58. http://dx.doi.org/10.1016/j.msea.2016.05.089.

[71] Segerstark A, Andersson J, Svensson L-E, Ojo O. Microstructural characterization of laser metal powder deposited Alloy 718. Mater Charact 2018;142:550–9. http://dx.doi.org/10.1016/j.matchar.2018.06.020.

[72] Sindhura D, Sravya MV, Murthy GVS. Comprehensive microstructural evaluation of precipitation in Inconel 718. Met Microstruct Anal 2019;8(2):233–40. http://dx.doi.org/10.1007/s13632-018-00513-0.

[73] Huang J, Huang Z, Du H, Zhang J. Effect of aging temperature on microstructure and tensile properties of Inconel 718 fabricated by selective laser melting. Trans Indian Inst Met 2022;75(6):1403–10. http://dx.doi.org/10.1007/s12666-021-02487-0.

[74] Guan H, Jiang W, Lu J, Zhang Y, Zhang Z. Precipitation of δ phase in Inconel 718 superalloy: The role of grain boundary and plastic deformation. Mater Today Commun 2023;36:106582. http://dx.doi.org/10.1016/j.mtcomm.2023.106582.

[75] Pearson K. Proc R Soc Lond 1895;58(347–352):240–2. http://dx.doi.org/10.1098/rspl.1895.0041.

[76] Spearman C. The proof and measurement of association between two things. Int J Epidemiol 2010;39(5):1137–50. http://dx.doi.org/10.1093/ije/dyq191.

[77] Kendall MG. A new measure of rank correlation. Biometrika 1938;30(1–2):81–93. http://dx.doi.org/10.1093/biomet/30.1-2.81.

[78] Niu X, He C, Zhu S-P, Foti P, Berto F, Wang L, et al. Defect sensitivity and fatigue design: Deterministic and probabilistic aspects in additively manufactured metallic materials. Prog Mater Sci 2024;144:101290. http://dx.doi.org/10.1016/j.pmatsci.2024.101290.

[79] Raßloff A, Schulz P, Kühne R, Ambati M, Koch I, Zeuner AT, et al. Accessing pore microstructure–property relationships for additively manufactured materials. GAMM-Mitt 2021;44(4). http://dx.doi.org/10.1002/gamm.202100012.

[80] Chen C, Xie Y, Yan X, Yin S, Fukanuma H, Huang R, et al. Effect of hot isostatic pressing (HIP) on microstructure and mechanical properties of Ti6Al4V alloy fabricated by cold spray additive manufacturing. Addit Manuf 2019;27:595–605. http://dx.doi.org/10.1016/j.addma.2019.03.028.

[81] El Haddad MH, Smith KN, Topper TH. Fatigue crack propagation of short cracks. J Eng Mater Technol 1979;101(1):42–6. http://dx.doi.org/10.1115/1.3443647.

[82] Santus C, Taylor D, Benedetti M. Experimental determination and sensitivity analysis of the fatigue critical distance obtained with rounded V-notched specimens. Int J Fatigue 2018;113:113–25. http://dx.doi.org/10.1016/j.ijfatigue.2018.03.037.

[83] Juvinall RC, Marshek KM. Machine component design. Wiley; 2012.

[84] Susmel L, Taylor D. A novel formulation of the theory of critical distances to estimate lifetime of notched components in the medium-cycle fatigue regime. Fatigue Fract Eng Mater Struct 2007;30(7):567–81. http://dx.doi.org/10.1111/j.1460-2695.2007.01122.x.

[85] Raghavendra S, Dallago M, Zanini F, Carmignato S, Berto F, Benedetti M. A probabilistic average strain energy density approach to assess the fatigue strength of additively manufactured cellular lattice materials. Int J Fatigue 2023;172:107601. http://dx.doi.org/10.1016/j.ijfatigue.2023.107601.

[86] Emanuelli L, Molinari A, Facchini L, Sbettega E, Carmignato S, Bandini M, et al. Effect of heat treatment temperature and turning residual stresses on the plain and notch fatigue strength of Ti-6Al-4V additively manufactured via laser powder bed fusion. Int J Fatigue 2022;162:107009. http://dx.doi.org/10.1016/j.ijfatigue.2022.107009.

[87] Benedetti M, Santus C, Raghavendra S, Lusuardi D, Zanini F, Carmignato S. Multiaxial plain and notch fatigue strength of thick-walled ductile cast iron EN-GJS-600-3: Combining multiaxial fatigue criteria, theory of critical distances, and defect sensitivity. Int J Fatigue 2022;156:106703. http://dx.doi.org/10.1016/j.ijfatigue.2021.106703.